2017

Simultaneous Imaging of the Diatomic Carbon and Methylidyne Species Radicals for the Quantification of the Fuel to Air Ratio from Low to High Pressure Combustion

Jonathan Reyes
University of Central Florida

SIMULTANEOUS IMAGING OF THE DIATOMIC CARBON AND METHYLIDYNE SPECIES RADICALS FOR THE QUANTIFICATION OF THE FUEL TO AIR RATIO FROM LOW TO HIGH PRESSURE COMBUSTION

by

JONATHAN ELIEL REYES
B.S. University of Central Florida, 2015

A thesis submitted in partial fulfillment of the requirements
for the degree of Master of Science
in the Department of Mechanical and Aerospace Engineering
in the College of Engineering and Computer Science
at the University of Central Florida
Orlando, Florida

Fall Term
2017

Major Professor: Kareem Ahmed

ABSTRACT

The radical intensity ratio of the diatomic carbon to methylidyne was characterized at initial pressures up to 10 bar using certified gasoline of 93% octane. This gasoline was selected due to its availability as a common fuel. The characterization of the radical intensity ratio of gasoline at elevated pressures enabled the creation of a calibration map of the equivalence ratio at engine relevant conditions.

The proposed calibration map acts as a feedback loop for a combustor. It allows for the location of local rich and lean zones. The local information acquired can be used as an optimization parameter for injection and ignition timings, and future combustor designs. The calibration map is applicable at low and high engine loads to characterize a combustors behavior at all points in its operation map.

Very little emphasis has been placed on the radical intensity ratio of unsteady flames, flames at high pressure, and liquid fuels. The current work performed the measurement on an unsteady flame ignited at different initial pressures employing a constant volume combustion chamber and liquid gasoline as the fuel source. The chamber can sustain a pressure rise of 200 bar and allows for homogenous fuel to air mixtures.

The results produced a viable calibration map from 1 to 10 bar. The intensity ratio at initial pressures above 5 bar behaved adversely in comparison to the lower pressure tests. The acquired ratios at the higher initial pressures are viable as individual calibration curves, but created an unexpected calibration map. The data shows promise in creating a calibration map that is useful for practical combustors.

This work is dedicated to all the hard-working graduate students at the propulsion and energy research laboratory. Your support is what has carried me this far. The group may be in its beginnings, but I take pride in the heart we share to make a lasting impression on the scientific community, regardless of whether the goal is achieved. It is my hope that you can learn from my work as I have learned from yours.

Thanks,

Jay

ACKNOWLEDGMENTS

The author would like to acknowledge, first and foremost, the almighty and only creator "I am" God. If not for His wondrous and beautiful mysteries, this work would not be possible. If not for my family (Rosa, Ismael, Joshua, and Jason Reyes), who raised me to always strive for higher standards, this would not be possible. Johanna Segura, your love and support through all of this is immeasurable. Abdiel Mendez, your theological and spiritual advice has carried me through so much and thanks are in order. Daniel Rodriguez, your life and moral advice has taught me to be a man and to take responsibility for my actions (good and bad). To my lab mates who contributed (Andres Curbelo, Wilmer Flores, Marissa Geikie, Dr. Ranjith Kumar, Michelle Otero, and Jonathan Sosa), I will forever be in debt to you, thank you. Last but most certainly not the least, I would like to acknowledge the one who initiated this study, Dr. Kareem Ahmed. Your knowledge of the subject has guided me every step of the way. You placed my academic growth above the terms of the project and I could ask for nothing more. A big thanks to you all.

TABLE OF CONTENTS

LIST OF FIGURES viii

LIST OF TABLES xi

LIST OF ACRONYMS (or) ABBREVIATIONS xii

CHAPTER ONE: INTRODUCTION 1

Background 1
The Development of Fuel Injection Systems for Automotive Engines 2
The Direct Injection Approach 5
CHAPTER TWO: LITERATURE REVIEW 9

The Radical Species 9
The Radical Intensity Ratio 10
Known Effects of Pressure on the Intensity Ratio 13
CHAPTER THREE: EXPERIMENTAL HARDWARE 15

Facility 15
Fuel Injection System 16
Data Collection System 18
CHAPTER FOUR: OPTICAL DIAGNOSTICS 20

Optics Overview 20
Image Splitter Design and Approach 21
Background Subtraction of CO2 24
CHAPTER FIVE: IMAGE PROCESSING 26

Processing Technique 26
CHAPTER SIX: FINDINGS 29

Validation 29
Temperature Effects 30
Calibration Map for Gasoline 30

CHAPTER SEVEN: CONCLUSION 37

LIST OF REFERNCES 38

LIST OF FIGURES

Figure 1: Main components of the traditional piston cylinder engine 2

Figure 2: Cut-out view of a carburetor with its main components labeled..... 4

Figure 3: Fuel injection comparison between (a) Port Injection and (b) direct injection 5

Figure 4: Charge modes for DI engines: (a) homogenous charger, (b) stratified charge 6

Figure 5: Common orientations used in charge stratification (a) spray guided, (b) wall guided, and (c) air guided 7

Figure 6: Operation map of generated torque and engine speed with the operation regions and their boundaries labeled for direct injection (DI) engines. 7

Figure 7: OH*, CH*, and C2* emitted intensity at various locations of a flame front; Φ=1.1 10

Figure 8: Spatially resolved spectra at various equivalence ratios denoting the location of various species radicals..... 11

Figure 9: Correlation of the chemilumiscent emission intensity ratio (log scale) and equivalence ratio comparing the results of using the peak intensity and the bandwidth for the measurement. 12

Figure 10: Schematic of the constant volume combustion chamber with its key components labeled 16

Figure 11: CVCC CAD design for high pressure modifications 16

Figure 12: Injector Shell and Injector Housing..... 17

Figure 13: Block diagram of Injector system with its key components labeled 18

Figure 14: Experimental facility with the key components labeled 18

Figure 15: Breakdown of instrumentation set up and its components on the CVCC 19

Figure 16: How the reacting mixture looks when the 427 nm ($CH*$ production) and 513 nm ($C2*$ production) filters are placed in the light path as viewed from the CVCC window. Images are not of the same event. 20
Figure 17: Diagram of beam optics inside image splitter casing. 22
Figure 18: Image Splitter casing with associated optics removed for viewing 22
Figure 19: Optical orientation for viewing through the optical access window 23
Figure 20: Optical orientation for endoscopic imaging 23
Figure 21: CO2* Broadband spectral emission 24
Figure 22: A breakdown of the image processing approach. From top to bottom and right to left: The target image, the flame image, the split images, the initial division, the mask to be applied, the divided image after background subtraction, noise reduction, and mask application. 27
Figure 23:An example of the Abel inversion technique applied to a methane-air flame on the $C2*$ filtered split image. Line of sight image is on the left and the deconvoluted image is on the right 28
Figure 24: Comparison of the results obtained from the experimental hardware and optical components of a propane-air and methane-air with Clark [9] and Jeong et al. [25] respectively 29
Figure 25: The effects of the initial temperature on the calibration curve for gasoline at an initial charge pressure of 1 bar. 30
Figure 26: Location of the data with respect to the combustion event. The graph shows a pressure trace of a combustion event. The initial peak is the point of ignition. The data is captured in the first 10 ms of the event. 31
Figure 27: An initial calibration curve for gasoline with various equivalence ratios shown. 32
Figure 28: Calibration curves for gasoline at select time steps after ignition. 33

Figure 29: The average of the curve fits of the data obtained in Figure 9. The curve fit is compared to Clark's [9] iso-octane data. Clark's iso-octane data is scaled to be on the same order as the gasoline data since the measurement is fuel specific..... 33
Figure 30: Calibration curves associated with charge pressures 1, 3, and 5 bar. The curve equation and correlation parameter are labeled for the respective curve fits. 34
Figure 31: Calibration curves associated with charge pressures 7 and 10 bar. The curve equation and correlation parameter are labeled for the respective curve fits. 35
Figure 32: Hypothesized calibration map for gasoline for charge pressures between 1 and 10 bar drawn from equation 4. 36
Figure 33: Simultaneous comparison of a pressure rise due to combustion and peak intensity of CH* at charge pressures of a.) 1.4, b.) 1.7, and c.) 2.0 MPa. 37

LIST OF TABLES

Table 1: List of Optical Components 25

LIST OF ACRONYMS (or) ABBREVIATIONS

CARBON DIOXIDE	CO_2
CARBON MONOXIDE	CO
CONSTANT VOLUME COMBUSTION CHAMBER	CVCC
DIATOMIC CARBON	C_2
DIRECT INJECTION	DI
ENGINE CONTROL UNIT	ECU
ENVIRONMENTAL PROTECTION AGENCY	EPA
EQUIVALENCE RATIO	Φ
ETHYLENE	C_2H_4
FUEL TO AIR RATIO	FAR
HYDROXYL	OH
METHANE	CH_4
METHYLIDYNE	CH
PORT FUEL INJECTION	PFI
PROPANE	C_3H_8
RADICAL SPECIES	*
SPARK IGNITION	SI

CHAPTER ONE: INTRODUCTION

Background

Carbon dioxide was declared a dangerous pollutant in 2009 by the Environmental Protection Agency (EPA) [1]. This brought forth massively complex and costly regulations that would hinder industries relying on fossil fuels. This caused congress to move forward with a cap and trade policy, and a climate treaty to hold the industry sector accountable for keeping EPA regulations [1]. Then President Barack Obama promised that " U.S. emissions in 2050 will be 83 percent below 2005 levels" [1]. That promise caused the industry to rush to produce lower fuel consuming machines and seek out alternative energy sources.

The rise of CO2 emissions has been an issue for quite some time. Sir Arthur Vick Obe reviews CO2 concentration (data organized by William Clark) in the earth's atmosphere from 1950-1982 [2]. The concentration was measured at various hemispheres and the data is reported in a statistical manner. It was estimated that if the growth rate of CO2 was to be maintained at 1.5 % per year, life would not be tolerable by the end of a century (2084) [2]. Fortunately, the average growth rate of CO2 has been maintained at 0.5 % from 1984-2014 [3], [4]. The effects of the policies set in motion in 2009 have yet to be realized.

This work will not go into much detail on the subject matter of geochemical consequences of increased greenhouse gases, but would like to highlight some areas of importance and impact. Consequences of continual rise of greenhouse gases are: a decrease in coral reef growth affecting ocean life, increased global temperatures (global warming/cooling) affecting plant life, and an effect on overall quality of life in the coming centuries [3]–[5]. The goal of this study is to create more efficient spark ignition (SI) engines ultimately reducing CO2 particulate emissions while simultaneously producing more energy per combustion cycle.

More specifically, this work's focus is on the automotive industry. As such, attention must be placed on the industries recent developments in emissions reductions. Since 1975, fuel economy has gone up by an average of 40 % [6] and the use of other alternative energy sources (wind, solar, etc.) has gone up by 10 % [7]. This is due mainly in part to the significant advances in engine design for increased performance [6].

The Development of Fuel Injection Systems for Automotive Engines

A traditional piston cylinder can be seen in Figure 1. The mechanics behind the design is that air is taken into the cylinder as the piston expands (or lowers), the air is then compressed as the piston rises, fuel is injected and ignited, the combustion event produces enough energy to push the piston downwards and expands the hot gases, the final upward stroke exhausts the hot gases [8].

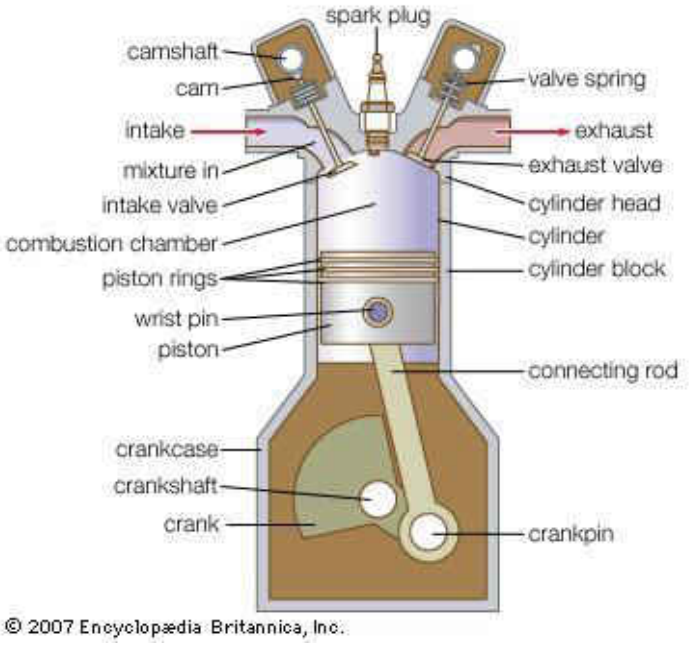

Figure 1: Main components of the traditional piston cylinder engine

Source: Encyclopedia Britannica
https://www.britannica.com/technology/piston-and-cylinder

The focus of this work lies in fuel injection and the characterization thereof. The end goal of a fuel injection design is to provide the desired fuel to air ratio (FAR) mixture inside the cylinder so that an efficient combustion can be obtained at all load conditions (cold start, high engine speeds, etc.). There are two main approaches to this: Premixing air and fuel before cylinder entry or mixing in cylinder. The radical intensity ratio measurement proposed will aid in the improvement of both systems. More attention is place on in cylinder mixing, though, since it has yielded greater power benefits over premixed [9]–[13].

Methods of fuel injection include the use of a pre-mixer/carburetor, injecting into the air intake port (port fuel injection, PFI), and injecting fuel directly into the cylinder (direct injection, DI) at specified timings [13]. A carburetor allows air to pass through a mixing chamber. As the air passes through the chamber fuel is drawn out from a separate channel and mixes with the incoming air, see Figure 2. The amount of fuel premixing is dictated mechanically by a throttle valve and carburetor chamber choke setting [14]. The premixed air and fuel are then injected into the cylinder and burned [14]. This is a crude manner of mixing but does not rely on any onboard computer systems [13].

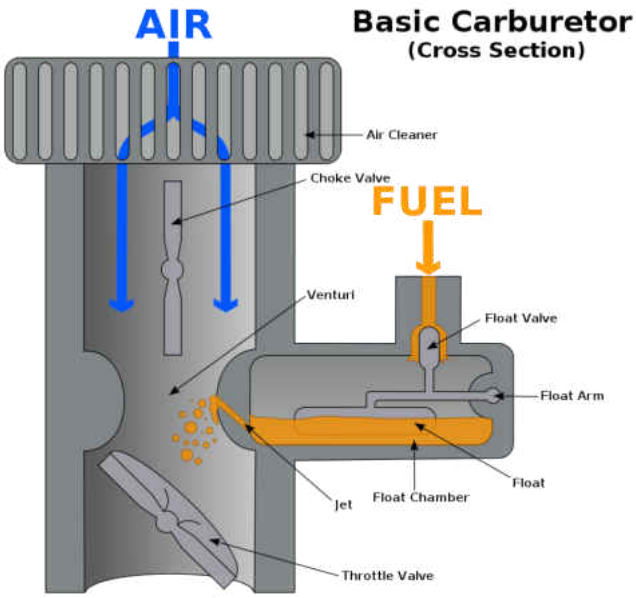

Figure 2: Cut-out view of a carburetor with its main components labeled

Source: K. Aainsquatsi, English Wikipedia publisher
https://en.wikipedia.org/wiki/Carburetor#/media/File:Carburetor.svg

Port fuel injection, whether single point (throttle body) or multi point (per cylinder), operate under the same approach as carburetors; in that, they inject fuel at some point before the cylinder and allow it to mix with the incoming air prior to entering the cylinder [15]. The difference is, that port fuel injection is controlled electronically with the use of an engine control unit (ECU) and various sensors to read mass air flow, engine speed, oxygen levels, throttle position, pressure, temperature, and voltage. The sensors, along with user input (steering angle, pedal depression, and gear) act as variables for the ECU to calculate the proper amount of fuel to be injected into the system and the rate and timing of each injection [15].

DI systems are controlled electronically in the same manner that PFI systems are controlled, the exception being that the injectors are mounted directly onto the cylinder to inject fuel into the cylinder [13], a comparison of PFI and DI orientations can be seen in Figure 3. This requires precise timing and efficient piston cylinder design [12], [13]. The benefits of injecting in such a manner are in increase in power and torque, but this technique also increases emission

particulates [10], [12], [13], [16]. This has caused engine manufactures to seek out a new design approach, in hopes of decreasing emissions to be comparable to that of a PFI system at standard operating temperatures. Recent developments in this area have been in piston head design, injector orientation, and fuel atomization [12], [13].

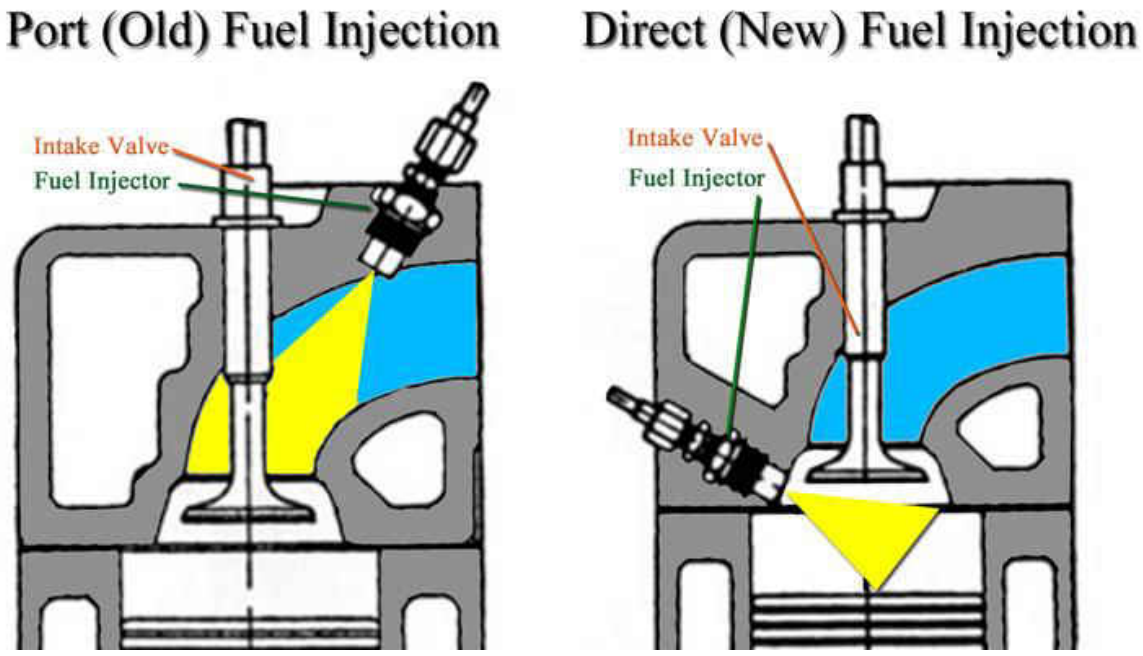

(a) (b)

Figure 3: Fuel injection comparison between (a) Port Injection and (b) direct injection

Source: Deutsche Autoparts [Doy-Chuh]
https://shopdap.com/fuel-injector-failures-on-volkswagen-2-0t-tsi/

The Direct Injection Approach

The goal would be to have the power and torque of a DI engine, and produce less emission particulates than PFI engines. Though, more complex, DI engines are ultimately preferred as it allows for better FAR control in all operation modes. PFI relies heavily on the intake system as a pre-vaporization chamber, which gives it an advantage for an engine at optimum temperature.

The DI combustion cycle relies on three main tuning parameters to achieve efficient combustion: Fuel atomization, injector timing (spray initiation and duration), and injector

orientation in conjunction with piston head design [10]–[13]. These parameters have led to three operation modes: stratified-charge, homogeneous lean, and homogenous stoichiometric [10]–[13]. There are various designs and injector timings that can be used, but these will not be discussed in depth as it is out of the scope of work, but in general stratified charges are used for light load conditions, homogenous lean is used for medium loads, and homogenous stoichiometric is used for high loads [13]. Figures 4, 5, and 6 show a breakdown of the various charge modes, spray designs, and a standard operation map respectively [13].

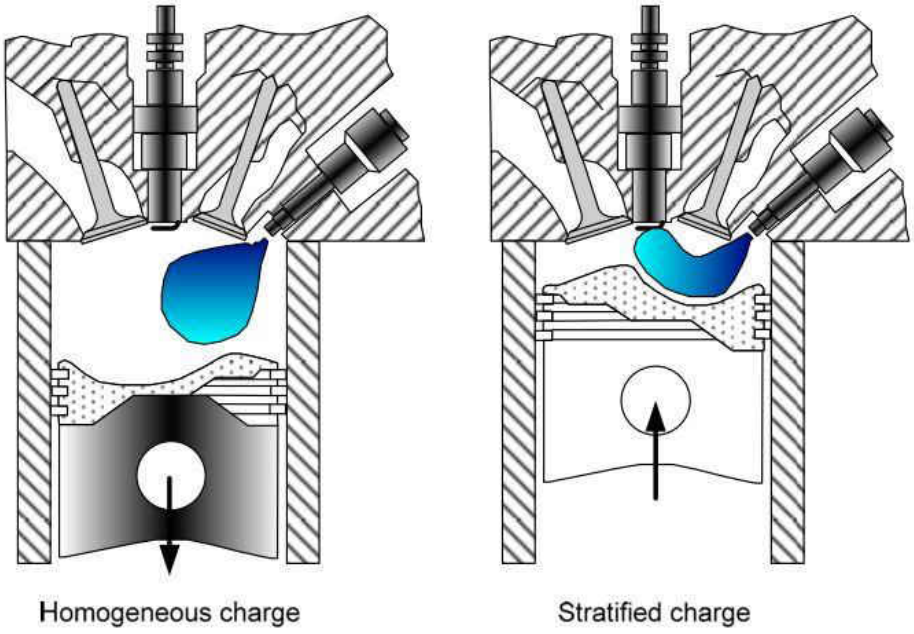

Figure 4: Charge modes for DI engines: (a) homogenous charger, (b) stratified charge

Source: [13]
https://www.intechopen.com/books/fuel-injection/gasoline-direct-injection

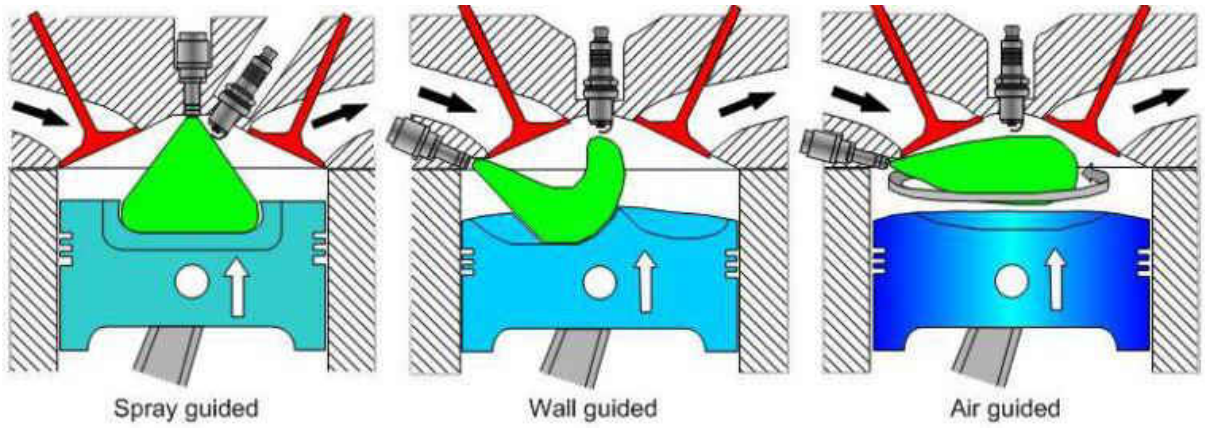

(a) (b) (c)

Figure 5: Common orientations used in charge stratification (a) spray guided, (b) wall guided, and (c) air guided

Source: [13]
https://www.intechopen.com/books/fuel-injection/gasoline-direct-injection

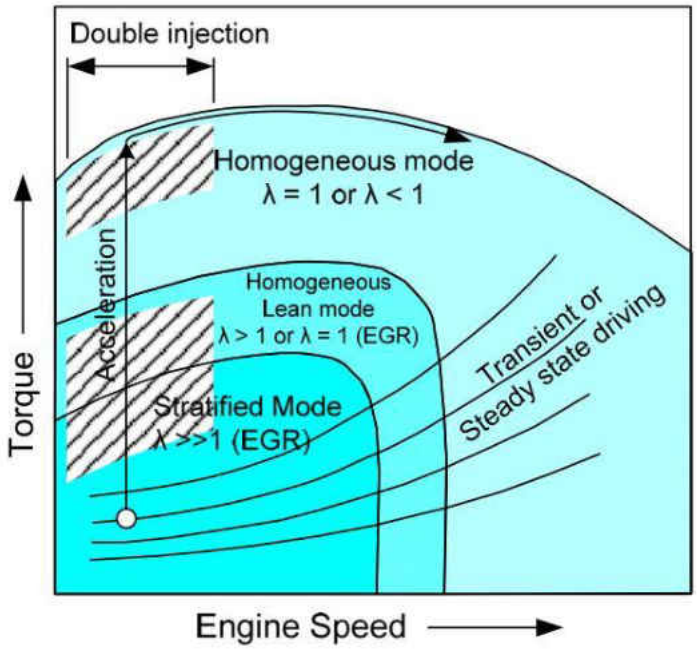

Figure 6: Operation map of generated torque and engine speed with the operation regions and their boundaries labeled for direct injection (DI) engines.

Source: [13]
https://www.intechopen.com/books/fuel-injection/gasoline-direct-injection

Increased particulate emissions in DI engines are mainly due to the stratified charge mode, where piston wetting can occur, increasing soot production and hydrocarbon emissions. Stratified

charges, though can be globally very lean, rely on local mixtures. In saying, the goal in a stratified charge is to provide a slightly fuel rich mixture at the spark plug, just prior to ignition, to initiate the combustion, and have the surrounding volume be lean [9], [12], [13]. Stratification is difficult to obtain at higher engine speeds limiting it to light engine loads [12], [13]. The stratified region on a standard operation map for DI engines, Figure 6, is between 25 and 30 % of the operation region, homogenous lean is between 10 and 15 %, and homogenous stoichiometric is between 55 and 65 % [9], [11], [13].

Since, 55 % of a driver's time is spent in the stratified operation region, the region with the most particulate emissions, better modeling, characterization, and design of combustion events associated with stratified charging is needed to improve the DI approach. Information on the local FAR, global FAR, soot and particulate development, and injection efficiency can be obtained during a combustion cycle. The purpose of this work is to obtain this information and characterize high pressure injectors used in DI engines.

CHAPTER TWO: LITERATURE REVIEW

The Radical Species

When a FAR mixture is ignited, the combustion events produces various products; namely, water (H_2O), carbon dioxide (CO_2), carbon monoxide (CO), diatomic carbon (C_2), hydroxyl (OH), and methylidene (CH) [17]–[21], all contained within a flame. The amount of each species produced is dictated mainly by the local FAR [17], [22]–[24]. Due to this correlation, in the 1950s it was proposed that the combustion product species radicals would be a valid measurement of the local FAR [17]. Radical meaning, a species that is highly reactive due to its electronic state (or unpaired valence electrons). Radical species will be denoted with a "*" for the remainder of this work.

Species radical intensities are a good indication of the location of the reaction zone of a flame [20], [21], [25], [26], the reaction zone being defined as the physical space in which the reactants (fuel and air) undergo a chemical change and produce new substances and heat. Referring to Figure 7, it is seen that the intensity emitted from a species radical is prevalent in both the unburned, and burnt region, but has a very defined peak at the location of the reaction zone [20]. Since species radicals consist of molecules with unpaired electrons, these species become highly reactive towards other substances and will often spontaneously dimerize or polymerize [27]. Meaning, the reaction zone contains a higher population count of these species radicals (and at a more excited state) than what is seen in other regions of the flame [17], [19]–[21], [23]–[30], thus emitting more light in those regions.

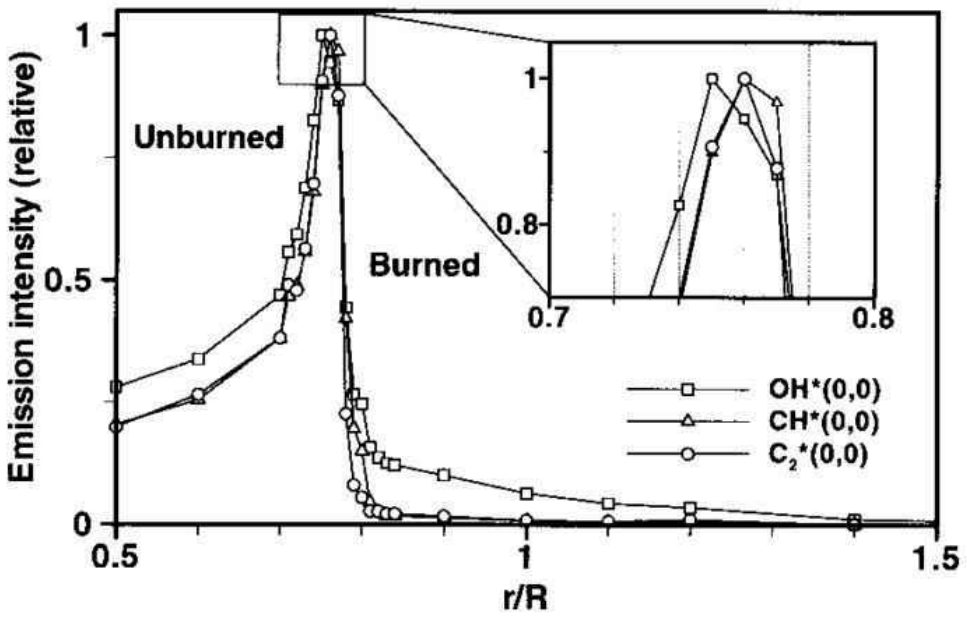

Figure 7: OH*, CH*, and C2* emitted intensity at various locations of a flame front; Φ=1.1

Source: [20]
http://www.sciencedirect.com/science/article/pii/S0082078400805779

The Radical Intensity Ratio

Each radical species has been found to emit light at specific wavelengths [20], [21], see Figure 8. Thus, "Local flame spectra can provide information on the chemistry of a local flame front" [20]. It has even been found that the band emissions related to each species radical can be used for understanding flame stoichiometry [17], [18], [20], [22], [24]–[26], [28]–[36].

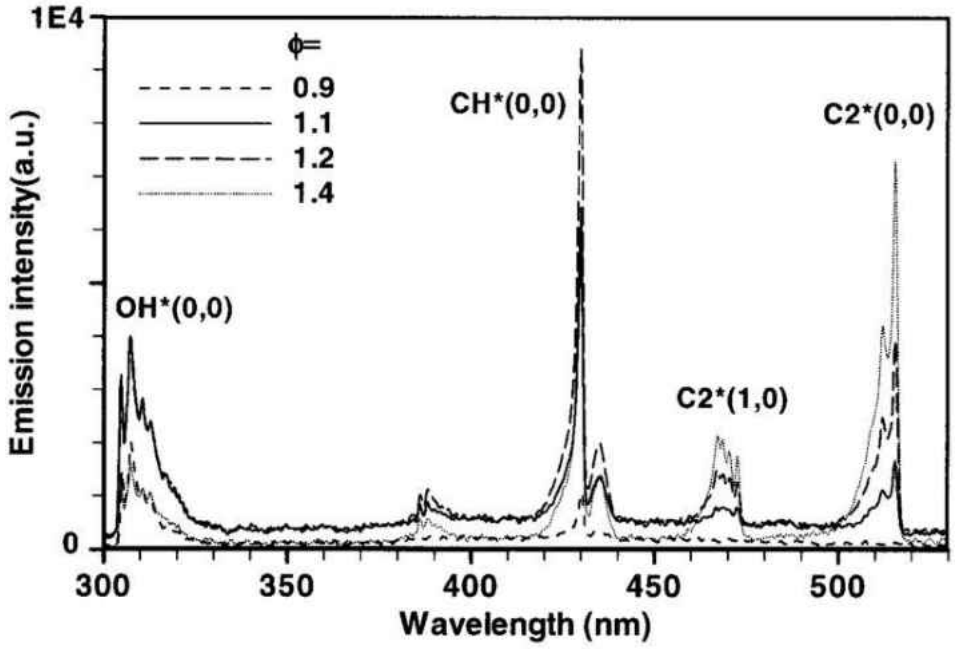

Figure 8: Spatially resolved spectra at various equivalence ratios denoting the location of various species radicals

Source: [20]
http://www.sciencedirect.com/science/article/pii/S0082078400805779

A correlation to the FAR can be made by taking the emitted intensity from a species radical and dividing it by the emitted intensity of another species radical, and comparing it to the FAR. Kojima set out to characterize the behavior of these ratios at various equivalence ratios from fuel-lean to fuel-rich, the results are documented in Figure 9; peak denotes maximum intensity value, band denotes the spectrally integrated emission of each band spectrum [20]. The ratio taken from the peak intensities and the full spectral band behave in the same manner with slight variations, and thus either approach to the method is valid [17], [18], [20], [22], [24]–[26], [28]–[36]. Kojima found that "The $\frac{C_2^*}{OH^*}$ curve is most sensitive to the equivalence ratio, and $\frac{C_2^*}{CH^*}$ is the next most sensitive. However, the correlations of $\frac{C_2^*}{OH^*}$ and $\frac{C_2^*}{CH^*}$ become less reliable for determining the local equivalence ratio for lean conditions…On the other hand, the correlation of $\frac{OH^*}{CH^*}$ is useful for

determining the equivalence ratio in lean premixed flames, because OH^* and CH^* emissions can be observed clearly in lean conditions" [20].

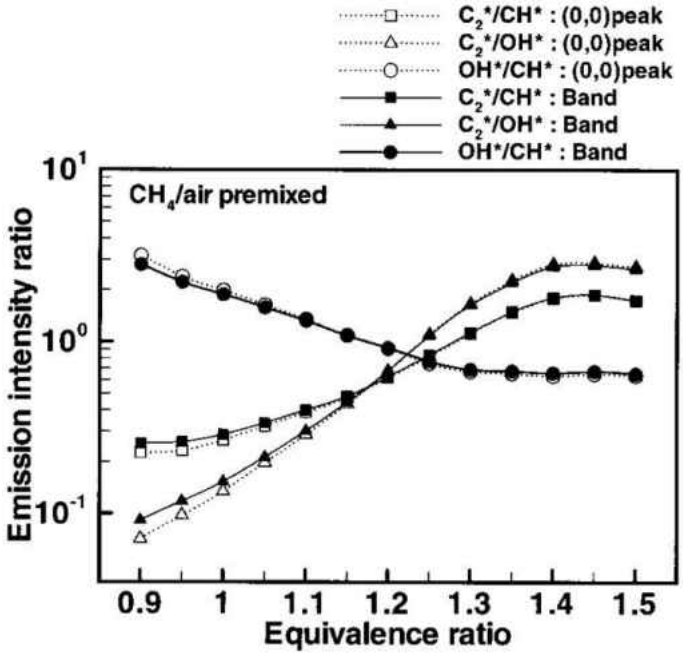

Figure 9: Correlation of the chemilumiscent emission intensity ratio (log scale) and equivalence ratio comparing the results of using the peak intensity and the bandwidth for the measurement.

Source: [20]
http://www.sciencedirect.com/science/article/pii/S0082078400805779

These behaviors, though, have been found to be fuel specific [17]. Kojima's study was done specifically with methane (CH_4) as the fuel source. Clarks' study consisted of propane (C_3H_8) and ethylene (C_2H_4) as fuel sources and found that the $\frac{C_2^*}{CH^*}$ was the more sensitive intensity ratio for the fuel sources, but notes that the sensitivity differs for each fuel source [17]. As such, for this study, the radical intensity ratio $\frac{C_2^*}{CH^*}$ will be used. This work primarily focuses on the detection of fuel-rich areas as seen in automotive DI engines, and will use gasoline as its fuel source for combustion, whose chemical formula (C_8H_{18}) is more closely related to that of propane [17], [22], [28], [30], [31], [33], [35]. It should be noted that the measurement, as discussed up to this point,

has been obtained using photomultiplier tubes or by chemiluminescence intensity. Both have yielded comparable results [20], [29], [30], [32].

Known Effects of Pressure on the Intensity Ratio

Automotive piston cylinders are built to operate at various speeds and charge pressures. The radical intensity ratio of $\frac{C_2^*}{CH^*}$ has yet to be fully characterized at various pressure levels comparable to that of a piston cylinder. T. Chou had performed a study utilizing in-cylinder measurements of C_2^* and CH^* to detect maldistributed FAR mixtures, but concludes that the measurement is load condition specific [28]. T. Fansler utilizes spark emission spectroscopy in a SI-DI engine as a means of determining local fuel concentrations, but notes that the technique suffers from spatial uncertainty [31]. Though, Fansler does report that re-calibration is not required if spark and fuel injection timing is changed [31]. B. Zigler proves that ignition phenomena of iso-octane, and gasoline based fuels can be accurately studied with the use of chemiluminesence, but does not measure FAR distribution [35]. J. Kim performed a study of the local heat release rate as correlated to combustor pressure, and found that there is a correlation of emission intensity of species radicals to pressure, but was limited to 30 kPa (or 0.3 bar), whereas automotive engines operate at much higher regimes (upwards of 140 bar) [37]. F. Tinaut performs a similar study as J. Kim, but instead uses a constant volume combustor [33]. Again, the highest pressure reported (2 MPa or 20 bar) is well below that of an automotive engine, but Tinaut does report that there is a dependence on pressure and temperature to emission intensity for n-heptane and iso-octane fuels [33]. Most recently, N. Kawahara improves upon the measurement by considering the suggestions made by T. Fansler, using an optical fiber to directly access the cylinder [22]. Kawahara reports that the species radical emission intensity can indeed be measured at high engine speeds (7000 RPM), but does not correlate these measurements to load conditions.

To summarize the previous work on the topic; all previous studies lead to the fact that it is possible to acquire emission intensities of various species radicals (C_2^*, CH^*, OH^*) at high engine loads and speeds, the radical intensity ratio approach is a valid correlation of the FAR, there is a pressure dependence on the radical intensity ratio, and that the system would not require recalibration if injection and spark ignition timings were to be changed. What is still lacking from the study is a well characterized calibration map that considers the combustion load conditions (pressure), the local equivalence ratios (FAR), and the emitted spectral intensities of the species radicals (radical intensity ratio) to standardize what is to be expected at all load conditions seen in an automotive piston cylinder. The calibration map can be used to visualize what areas of a combustion event coincide with local fuel-rich and fuel-lean regions and its overall development over time. It can be used as a means of tracking soot production, and ultimately be used as a feedback system (using the previous FAR as the input), to adjust injection/spark tuning parameters, and can help guide future piston cylinder hardware designs. Such a calibration map will also aid computational models on the subject, creating more accurate combustion species models.

CHAPTER THREE: EXPERIMENTAL HARDWARE

Facility

To complete the task of creating a calibration map that accounts for FAR, radical species intensity ratio, and pressure, a constant volume combustion bomb is employed for its simplicity and ease of instrumentation [33]. The constant volume combustion chamber (CVCC) is instrumented with a heat strap for facility temperature control, a dynamic pressure transducer, a thermocouple, an automotive high pressure gasoline injector, an oxygen sensor, a spark plug, a port for endoscopic imaging, and an optically accessible window, see Figure 10. The combustion chamber, itself, was inherited from a previous study and was left to rust in a shed behind building 44 at the University of Central Florida. The two-liter chamber was not originally built to handle pressures above 150 bar, so the chamber was rewelded and modified to withstand pressures up to 200 bar using a factor of safety of 7 (burst pressure of the DBLE. E.H. stainless steel pipe is rated at 1,400 bar), see Figure 11. The facility was equipped with two recessed flanges in which a three-quarter inch pressure rated tempered borosilicate glass sits capable of handling a 200 bar load.

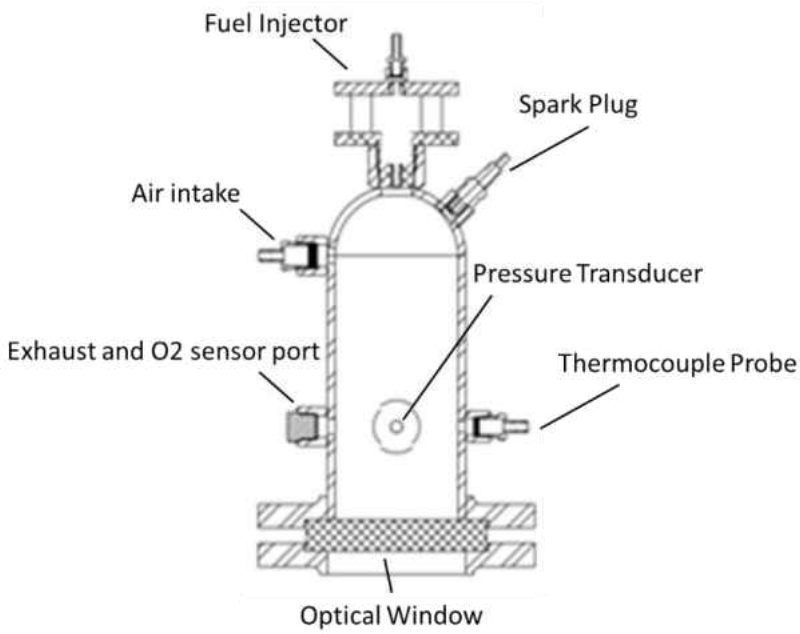

Figure 10: Schematic of the constant volume combustion chamber with its key components labeled

Figure 11: CVCC CAD design for high pressure modifications

Fuel Injection System

The fuel injector used is a proprietary gasoline direct injector supplied by Continental Automotive Systems, Virginia. The details of the injector cannot be discussed in this work, a mock

drawing of the injector shell and housing will be provided as a means of representation. It should be stated, though, that the injector provides adequate atomization with a cone angle wide enough to cover the volume without wall deposition. The injector sits in a custom-made housing that provides and fills the injector with fuel, completely seals the injector from any foreign matter besides fuel, can withstand fuel pressure above 100 bar, and can withstand the combustion pressure (200 bar), see Figure 12. The injector is controlled using an engine control unit (ECU) supplied by continental automotive systems and a Berkeley Nucleonics Corp Model 575 Digital Delay/Pulse Generator. Injection rate and duration is set using the delay generator, the signal is sent to the ECU to be converted into the signal required to excite the electromagnet in the injector. The fuel for the injector is delivered by a Haskel Air Driven Liquid Pump (0.75 Horsepower, Model 4B) at a pressure of 100 bar which is sufficient for atomization. A block diagram of the fuel injector hardware loop can be seen in Figure 13. Figure 14 shows the actual system.

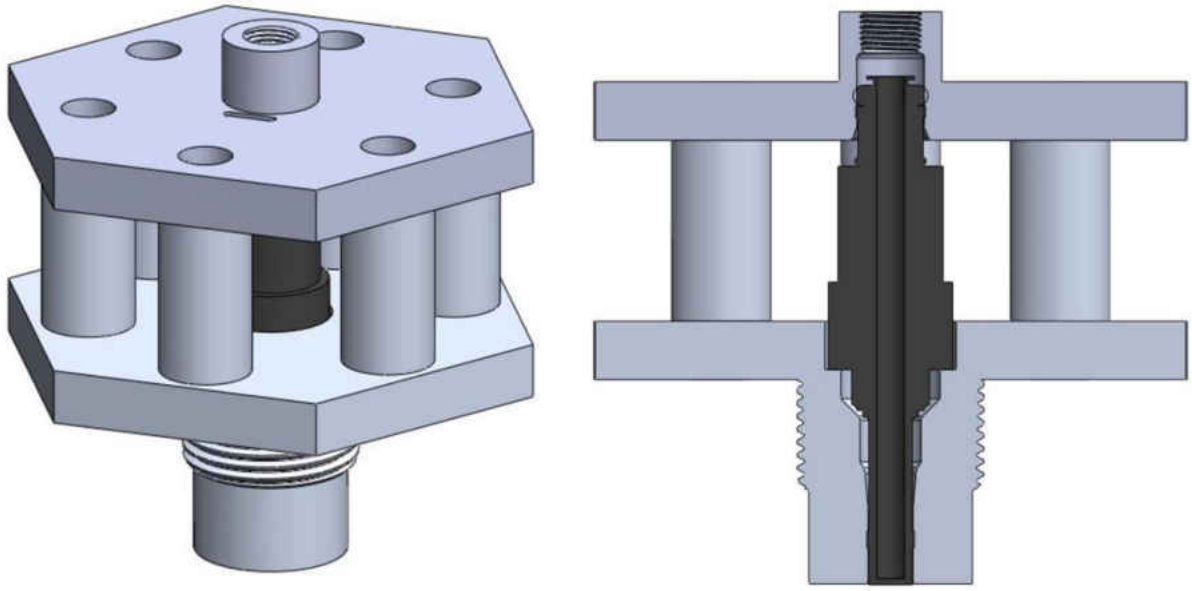

Figure 12: Injector Shell and Injector Housing

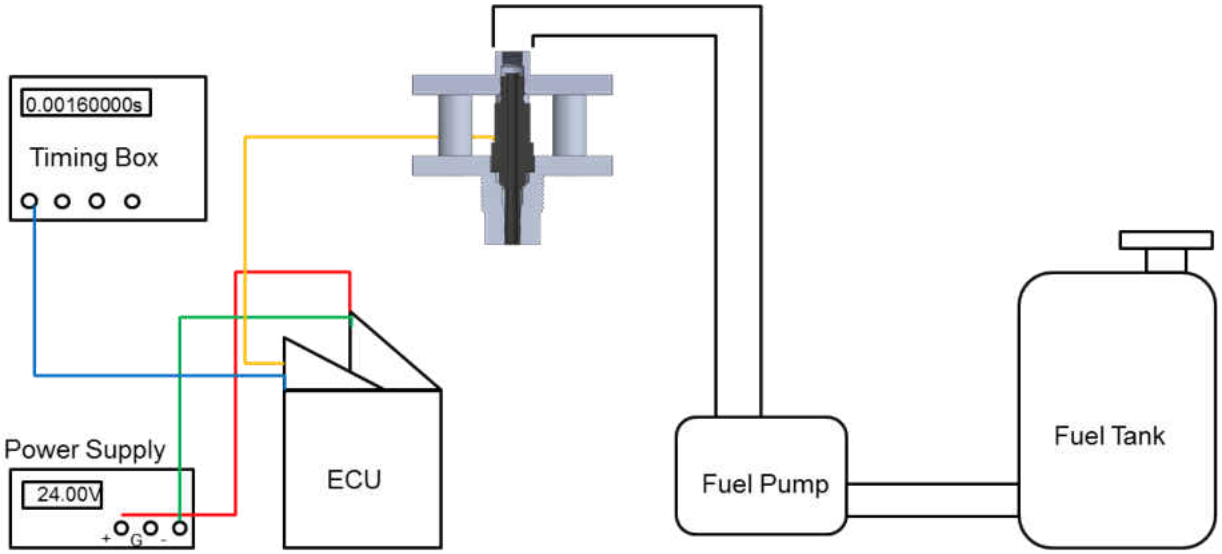

Figure 13: Block diagram of Injector system with its key components labeled

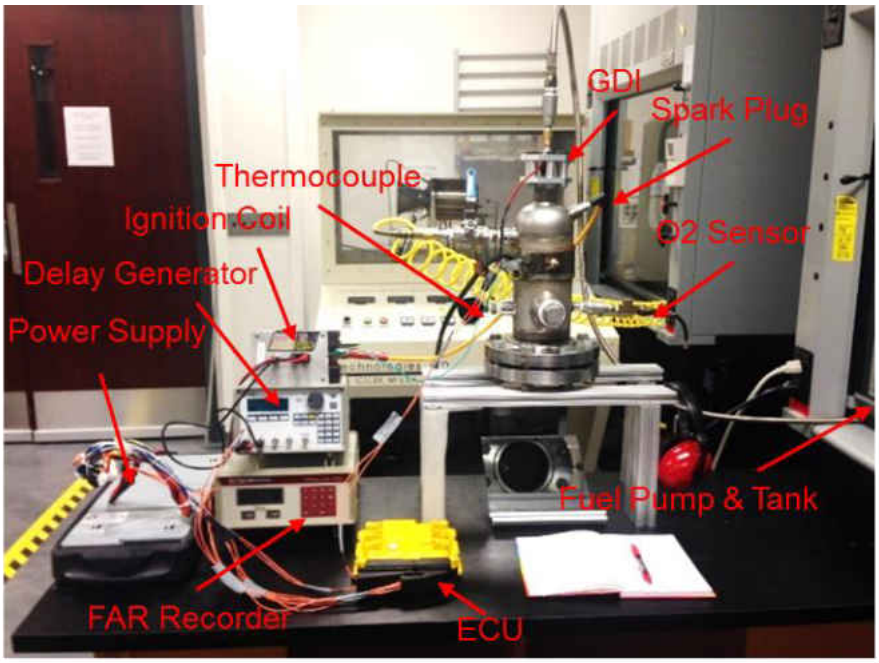

Figure 14: Experimental facility with the key components labeled

Data Collection System

An Omega TJ36 K-Type thermocouple was chosen due to its heavy-duty build, capability of handling the 200 bar load, its error limit of 0.75 %, and response time of 1 second for small changes in temperature (1-5 degree Celsius) and 10 seconds for large jumps in temperature (100

degrees Celsius). A Kistler Type 6061B cylinder pressure sensor was used to capture pressure rises seen inside the CVCC. The pressure sensor has a range of 0-250 bar, has a sensitivity of 25 pC per bar, and a maximum error of 0.2 bar under thermos shock conditions. The facility was heated by an external heat strap which could heat up to 100 ± 5 degrees Celsius. An ECM AFRecorder 2000 was used to measure the FAR of the exhaust gases. This is done by measuring the oxygen concentration in the exhaust gases and comparing it to the oxygen concentration in the ambient air. This serves as a global FAR measurement. It has a range of $0 \leq \Phi \leq 2.5$, has an accuracy of ± 0.9 % of the FAR measurement, and has a response time less than 150 ms. Ignition is initiated through an automotive ignition coil that has been retrofitted to work off a standard TTL signal. This allows for the precise control of when the mixture is ignited and sets the timing for all other instrumentation. A breakdown of the instrumentation set up can be seen in Figure 15 and an actual representation can be seen in Figure 14.

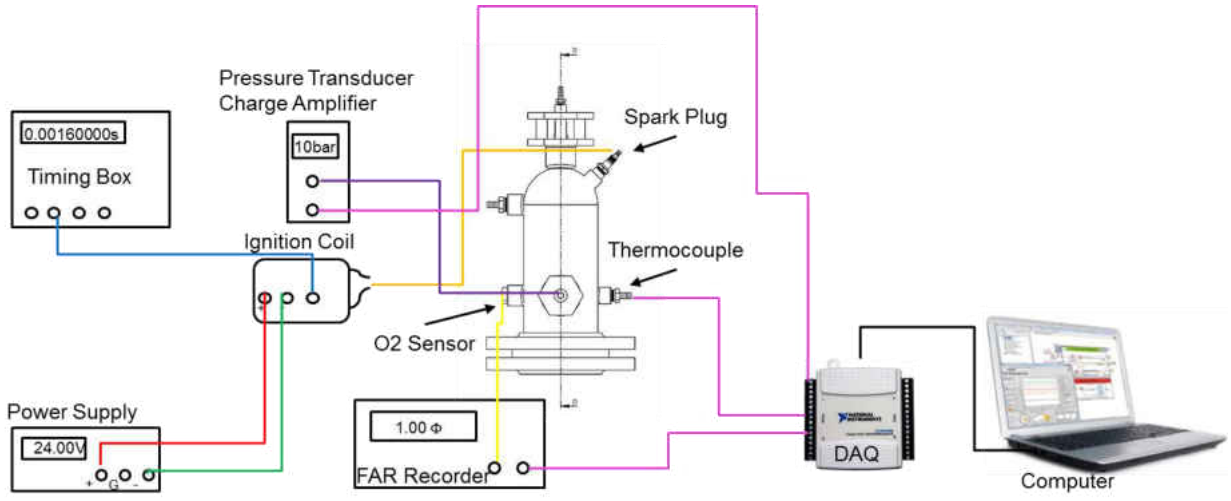

Figure 15: Breakdown of instrumentation set up and its components on the CVCC

CHAPTER FOUR: OPTICAL DIAGNOSTICS

Optics Overview

As discussed in chapter two, it is more beneficial to visualize the production of C_2^* and CH^* in fuels with a higher carbon count. The goal is then to simultaneously visualize the production of both radical species without the need of separate views. This allows for a line of sight visual inspection of the combustion event, and acts as a means of accurately obtaining the radical intensity ratio $\frac{C_2^*}{CH^*}$.

Refer to Figure 8, the CH^* species emits on a wavelength band of 420 to 440 nm, or violet light, and the C_2^* species radical emits on a wavelength band of 500 to 520 nm, or green light. The C_2^* species also emits on a wavelength band of 460 to 475 nm, but it has been shown to have very weak emittance at those wavelengths [20]. An example of this can be seen in Figure 16 where three separate images are taken, one with no filters, one with a 427 nm filter, and one with a 513 nm filter. In simpler terms, to acquire the radical species intensity ratio, the intensity of the green image is divided by the intensity of the blue image seen in Figure 16.

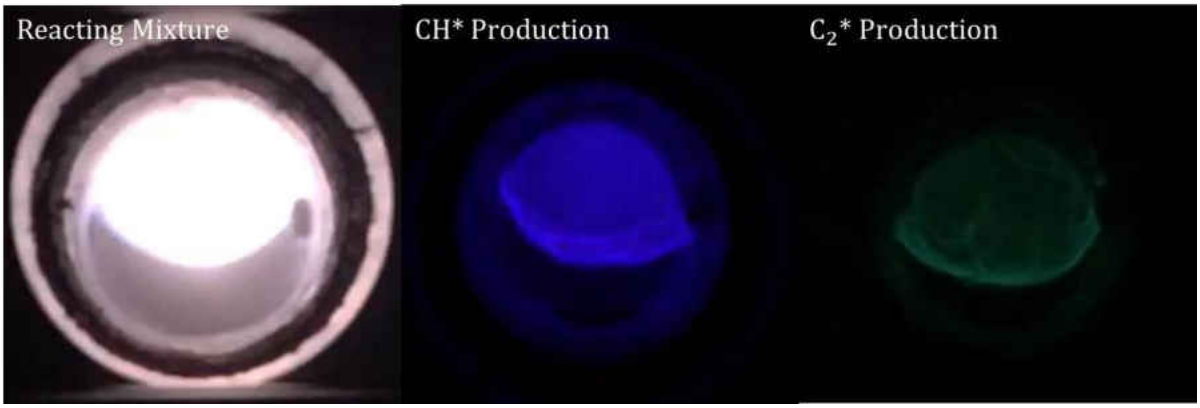

Figure 16: How the reacting mixture looks when the 427 nm (CH^* production) and 513 nm (C_2^* production) filters are placed in the light path as viewed from the CVCC window. Images are not of the same event.

Image Splitter Design and Approach

To perform this task simultaneously with the use of one camera, beam optics are employed. P. Toh describes in his patent, a method in which various wavelengths of an object being viewed can be acquired simultaneously using dichroics and short pass filters [38]. He proceeds to propose an apparatus which encases all necessary optics which could then be used to place in front of any image sensor [38]. Aggarwal and Ahuja proceed to test the idea and find that, indeed, it is a viable and useful tool that can be used to extract wavelength specific information of the same event, the sacrifice being the resolution of the image [39]. Essentially, the image sensor of a camera can be split into various quadrants (dependent upon the number of wavelengths being viewed) and a wavelength specific image can be projected onto one of the quadrants (whereas, to the camera it will be one image). The array of associated optics required to extract wavelength specific information and project it onto a quadrant of an image sensor will be referred to as an image splitter. Since C_2^* and CH^* are the only species of interest, only a 2-channel (two quadrant) image splitter is required. A diagram of the splitter and its associated optics can be seen in Figure 17 and an image of the actual casing for the optics can be seen in Figure 18. The steering mirrors depicted in the diagram allow for ease of alignment and placement of the image to be projected onto the image sensor. A fiber wound bundle is attached to the end of the image splitter allowing the optics to be placed away from the experimental facility for ease of alignment. A schematic of the optical set up can be seen in Figure 19 where the glass window is used. Figure 20, shows the optical setup when endoscopic imaging is used. The varying optical approaches allow for a look at the initial flame kernel produced from the spark plug (endoscopic), and the unsteady flame propagating through the facility (optical access window).

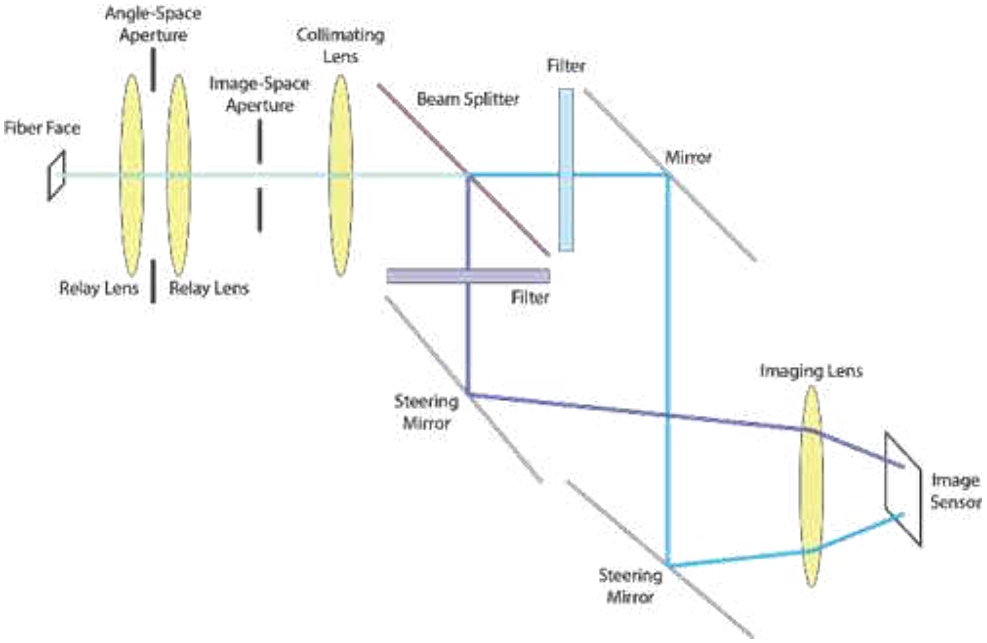

Figure 17: Diagram of beam optics inside image splitter casing.

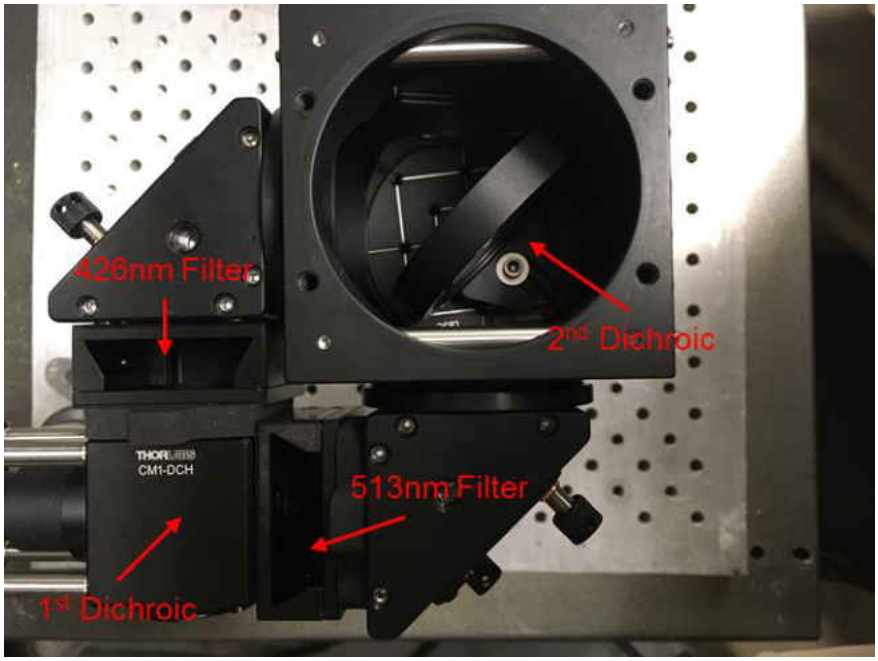

Figure 18: Image Splitter casing with associated optics removed for viewing

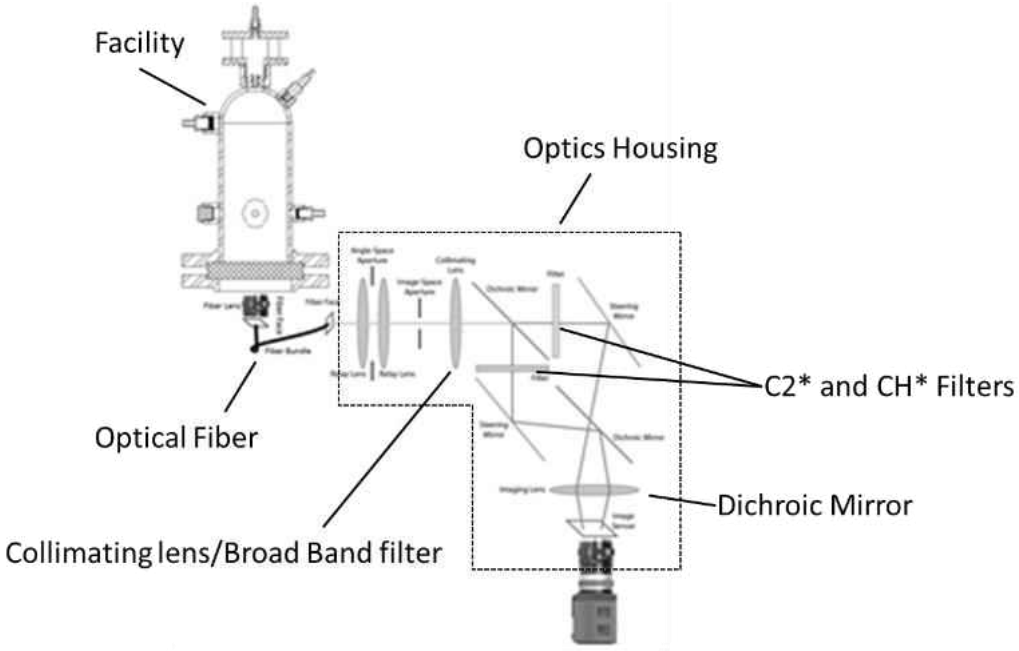

Figure 19: Optical orientation for viewing through the optical access window

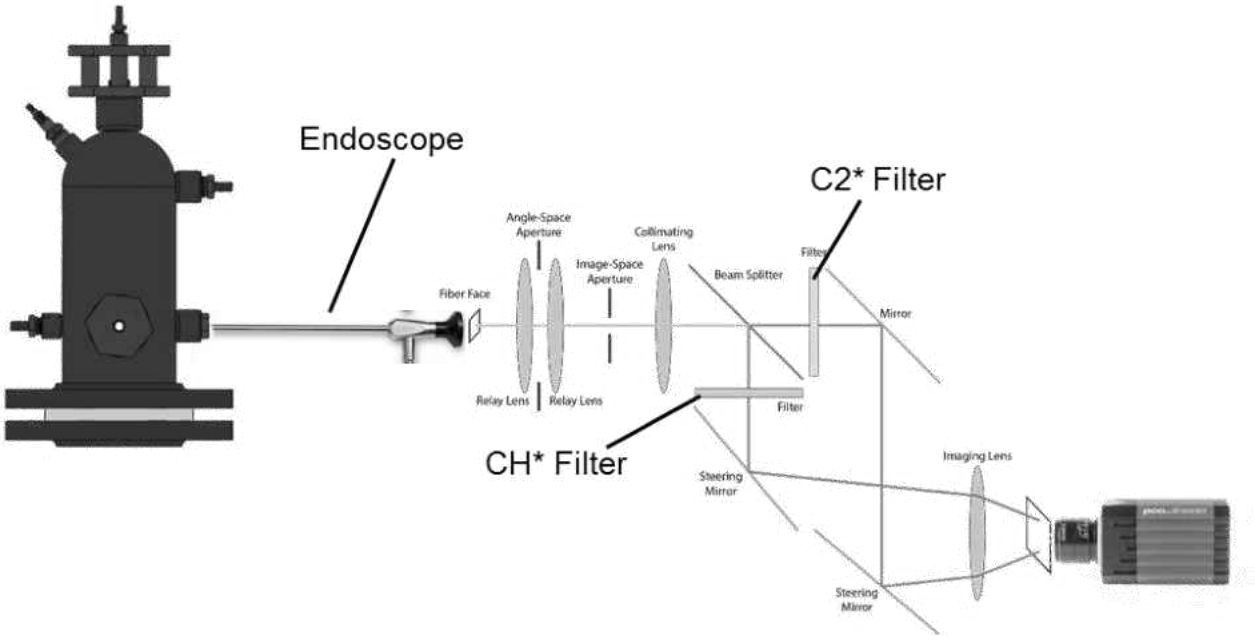

Figure 20: Optical orientation for endoscopic imaging

Background Subtraction of CO2

One of the inherent issues with this measurement is the emission of CO_2^*. CO_2^* emits on a wide range of wavelengths (300 to 600 nm), also known as broadband emissions [40], see Figure 21. This could cause CO_2^* to contribute to either C_2^* or CH^* intensity measurements and skew the results. To correct for this, a broadband filter covering the same region as the emitted region of CO_2^* is placed just before the splitter as a means of subtracting the signal from the incoming light. This lowers the overall intensity of the C_2^* and CH^* signals, but allows for clarity when visualizing the C_2^* and CH^* radical species. Table 1 contains a list of the optics used, their specifications, and their intended use.

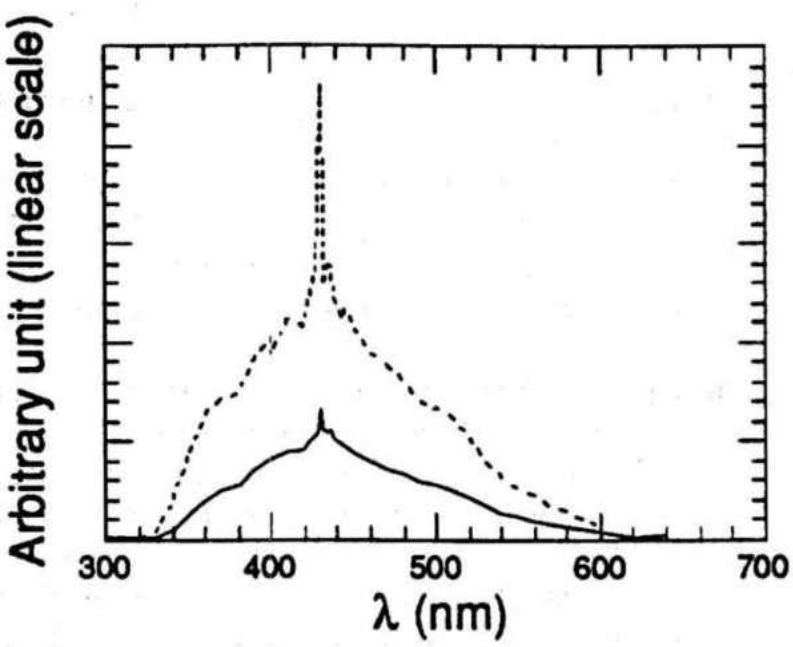

Figure 21: CO2* Broadband spectral emission

Source: [40]
http://www.tandfonline.com/doi/abs/10.1080/00102209508951901

Table 1: List of Optical Components

Optical Component	Specifications	Intended Use
Semrock FF484 Dichroic	98% Transmission for $\lambda > 484$ nm 98% Reflectance for $\lambda < 484$nm	To direct light onto Image Sensor of Camera
Semrock FF01-513 Bandpass Filter	95% Transmission for $504.5 < \lambda < 521.5$ nm	Viewing C_2^* Bandwidth
Semrock FF01-427 Bandpass Filter	95% Transmission for $422 < \lambda < 432$ nm	Viewing CH^* Bandwidth
Semrock LP03-32 Long-pass Filter	90% Transmission for $327 < \lambda < 733$ nm	CO_2^* Signal to be subtracted

To summarize, the above approach allows for the simultaneous capture of both the C_2^* and CH^* signals at the sacrifice of resolution, it is adaptable for use with endoscopic imaging, and accounts for the contribution of CO_2^* broadband spectral emission. The use of a fiber wound bundle allows the optics to be placed away from the experiment if necessary. The steering mirrors, allow the case to be adaptable to various image sensor sizes. Finally, optical components allow for minimum light loss, with the max light loss in the system being 10 % through the broadband filter, and the final light loss through all optics on each light path being 16 %. This was calculated with equation 1 where T_n (with n=1,2,3…) is the respective optical component light transmission.

$$Total\ Light\ Loss\ (\%) = 100(1 - (T_1 * T_2 * T_3 \ldots * T_n)) \quad (1)$$

CHAPTER FIVE: IMAGE PROCESSING

Processing Technique

An initial target image is taken and is used to ensure that there is a proper pixel to pixel comparison. The target image is removed from the plane of focus and is replaced by a flame at a given equivalence ratio. An image of the flame is acquired from both channels of the splitter and are cropped by utilizing the target images. Patterns detected in one side of the target image are searched for in the other side. A crop region is created and applied to both sides of the split image. This crop location is applied to all subsequent flame images. The cropped images' intensity values are used to extract the radical intensity ratio by dividing the C_2^* image's intensity values by the CH^* image. The division of the radical species chemiluminescence can produce unwanted background noise. Thus, techniques such as background subtraction, adaptive masking, and noise reduction were employed. A breakdown of the process can be seen in Figure 22 where the technique is applied on a gasoline-air mixture initial flame kernel at an equivalence ratio of unity. This process is repeated for various equivalence ratios. The intensity ratios are plotted against the equivalence ratio to arrive at a calibration curve.

The above approach is a line of sight calculation of the chemiluminescence intensity ratio. The line of sight approach, though has proven to yield accurate results, does not account for the spatial distribution of a flame [17], [36]. A deconvolution technique known as the Abel inversion algorithm utilizes the axisymmetric nature of the flame to project 2D planar information. In other words, half of the line of sight data can be used to understand the flames characteristics in another 2-D plane assuming it is axisymmetric. This allows for an accurate depiction of the reaction zone. Given a spherically symmetric function the Abel transform can be written as

$$F(y) = 2\int_y^\infty \frac{f(r)rdr}{\sqrt{r^2-y^2}} \tag{2}$$

The inversion of the Abel transform allows for the recovery of the symmetrical field distribution by using the projected data. If f(r) arrives at zero faster than 1/r the inverse transform is given by

$$f(r) = \frac{1}{\pi}\int_r^\infty \frac{dF}{dy}\frac{dy}{\sqrt{y^2-r^2}} \tag{3}$$

The inversion algorithm was performed on a line of sight image of a methane-air flame's C_2^* emission exhausting to atmosphere at an equivalence ratio of unity. The deconvoluted image shows a clear representation of the reaction zone location, see Figure 23.

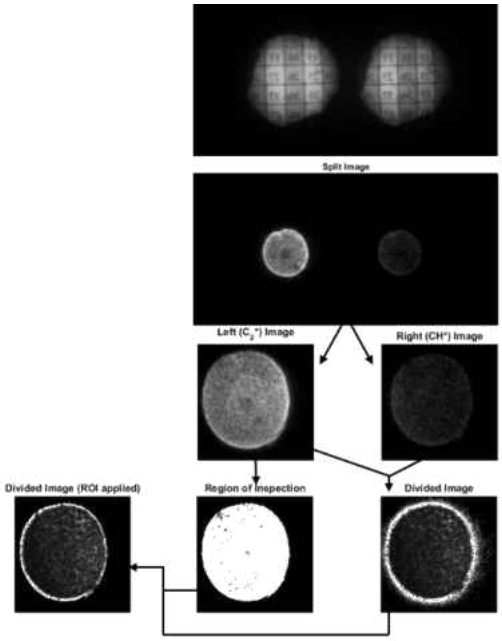

Figure 22: A breakdown of the image processing approach. From top to bottom and right to left: The target image, the flame image, the split images, the initial division, the mask to be applied, the divided image after background subtraction, noise reduction, and mask application.

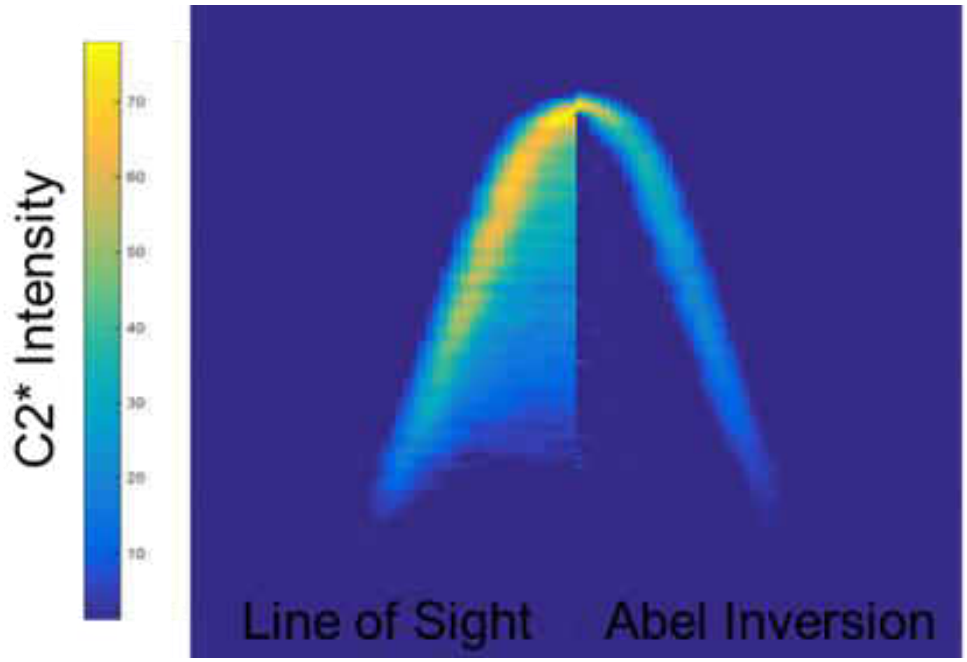

Figure 23:An example of the Abel inversion technique applied to a methane-air flame on the C_2^* filtered split image. Line of sight image is on the left and the deconvoluted image is on the right

CHAPTER SIX: FINDINGS

Validation

Split images of steady methane-air and propane-air flames were taken to assess the validity of the system. The propane-air and methane-air results were compared to the data obtained by Clark [17] and Jeong *et al*. [36]. The fuel to air ratio for the validation experiment was controlled using Dwyer Series MM flowmeters with a resolution of 0.1 SCFH. The fuel and air mixture was stabilized using a Humboldt natural gas burner with a 12 mm diameter circular exit plane. 20 images were taken at each equivalence ratio point and used to acquire the average of the intensity ratio at that location utilizing the proposed image processing technique. The results of the comparison test can be seen in Figure 24. The deviation associated with the average intensity ratio is ± 0.3 which is comparable to what has been reported in both Clark's [17] and Jeong's *et al*. [36] work.

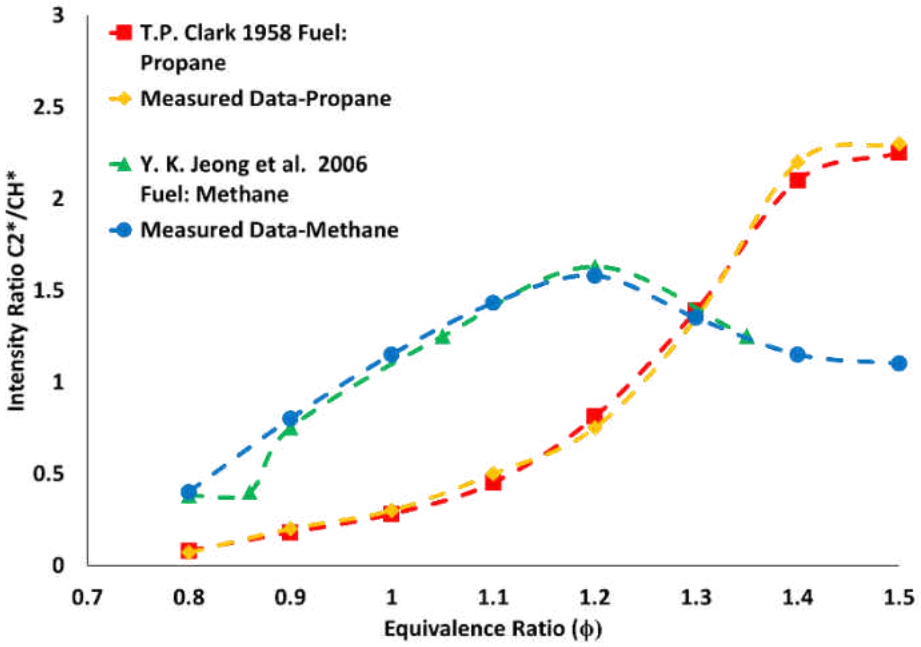

Figure 24: Comparison of the results obtained from the experimental hardware and optical components of a propane-air and methane-air with Clark [9] and Jeong *et al*. [25] respectively

Temperature Effects

Temperature is known to affect the production and emission of the radical species. A test was conducted utilizing the constant volume combustion chamber to record the effects the initial temperature had on the measurement. The effects can be seen in Figure 25. To be sure that the effects of the initial charge pressure are being isolated correctly all results pertaining to the calibration map are of an initial charge temperature of 60 °C.

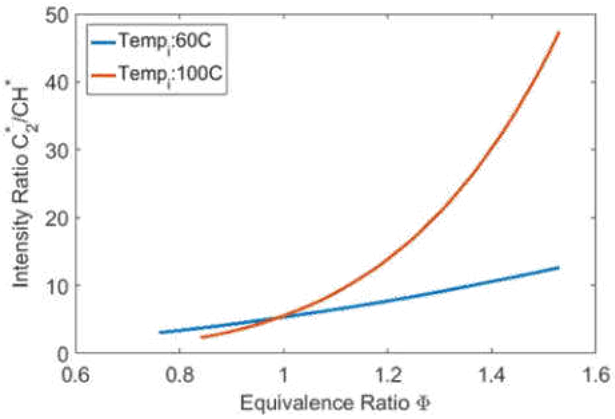

Figure 25: The effects of the initial temperature on the calibration curve for gasoline at an initial charge pressure of 1 bar.

Calibration Map for Gasoline

Because of the constant volume combustion chamber's 2 liter volume the pressure rise due to combustion takes about 400 ms to reach its peak. This allows for ample time to record the effects of initial charge pressure on initial flame kernel. Figure 26 is a pressure trace of a combustion event of an initial charge pressure of 2 bar. Marked in red is the location were data is to be extracted. The initial spike seen is the point of ignition. Between 30 and 100 frames were extracted for the calculation of the intensity ratio in this region depending upon the frame rate of the camera. The resolution of the images was 0.4 megapixels, meaning each split image had a resolution of 0.2

megapixels. The marked location in Figure 26 has a time duration of 10 ms. The pressure rise due to combustion in this region is 0.1 bar.

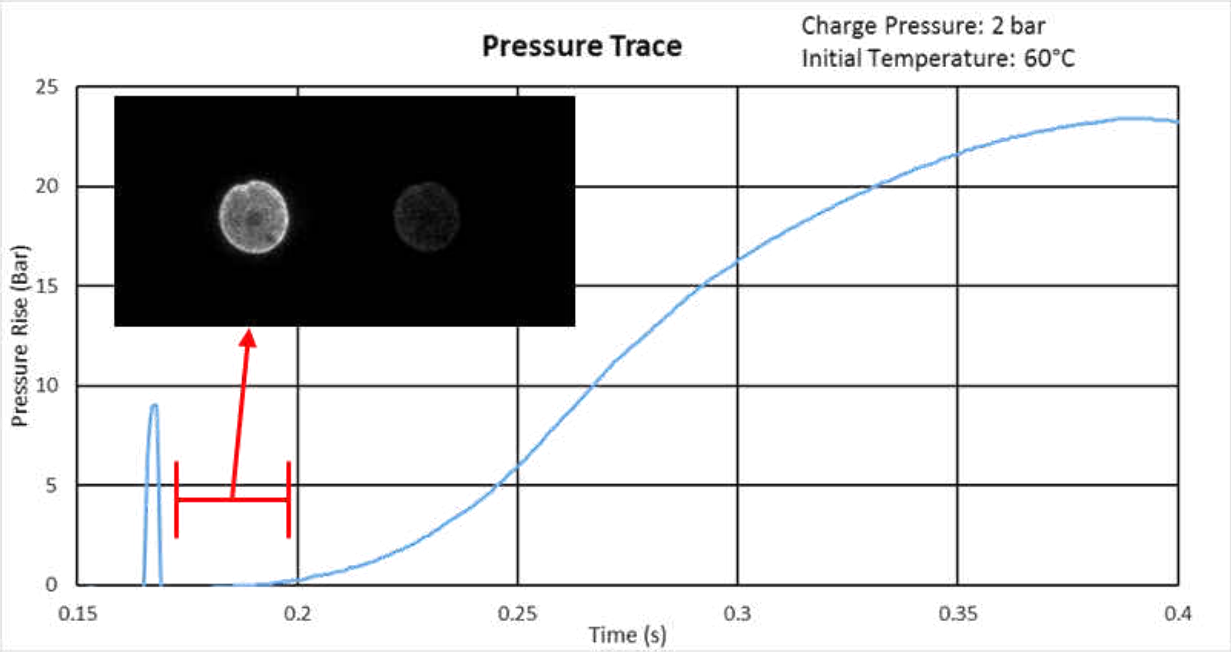

Figure 26: Location of the data with respect to the combustion event. The graph shows a pressure trace of a combustion event. The initial peak is the point of ignition. The data is captured in the first 10 ms of the event.

A scatter plot was drawn from the data obtained using the gasoline fuel at a charge pressure of 1 bar and was found to behave in the manner seen in previous works [17], [29], [32], [36]. The calibration curve behaves as a power curve, Figure 27, with an average uncertainty of ± 0.518 in the calculation of the intensity ratio at a given equivalence ratio. The uncertainty of the average intensity ratio at a given equivalence ratio at each time step was ± 0.03.

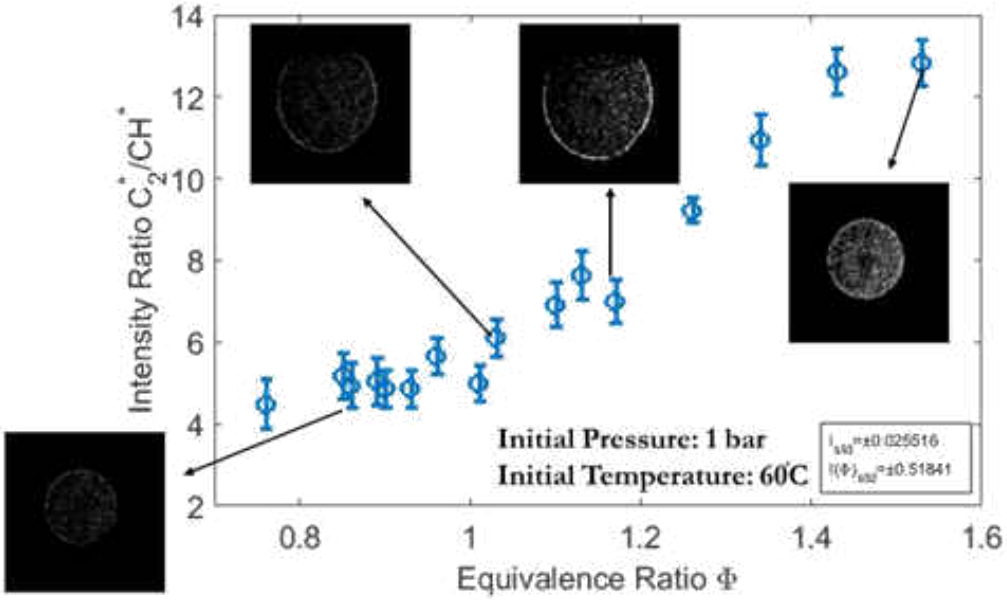

Figure 27: An initial calibration curve for gasoline with various equivalence ratios shown.

A calibration curve was drawn for each time step. Figure 28 demonstrates this and shows that there is a slight effect on the curve as the pressure begins to rise over time. As time increases the calibration curve begins to shift. The pressure rise recorded in the first 10 ms after ignition, as mentioned, is 0.1 bar. Thus, even the pressure rise at the initial flame kernel has a slight effect on the measurement. To mitigate this effect, an average of all the calibration curves at each time step was taken and reported. The curve shown in Figure 29 is a result of the data in Figure 28 averaged. The average correlation coefficient (R) was 0.98, showing good agreement to its behavior as a power curve. Because this measurement is fuel specific, to compare the trend seen with gasoline fuel, Clark's iso-octane data was scaled and overlaid onto the calibration curve for gasoline. The data in Figure 29 shows good agreement in the calibration curve's trend.

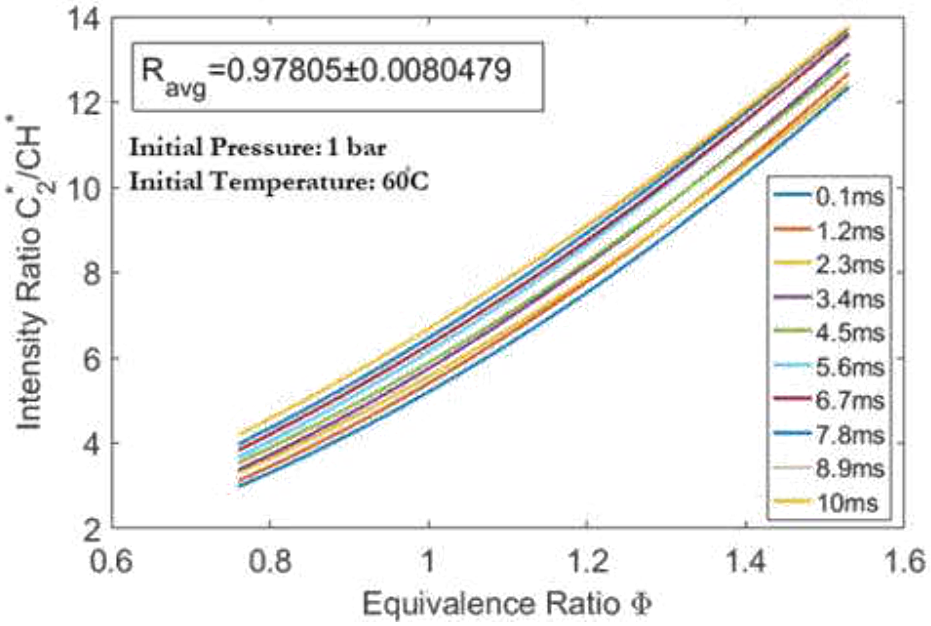

Figure 28: Calibration curves for gasoline at select time steps after ignition.

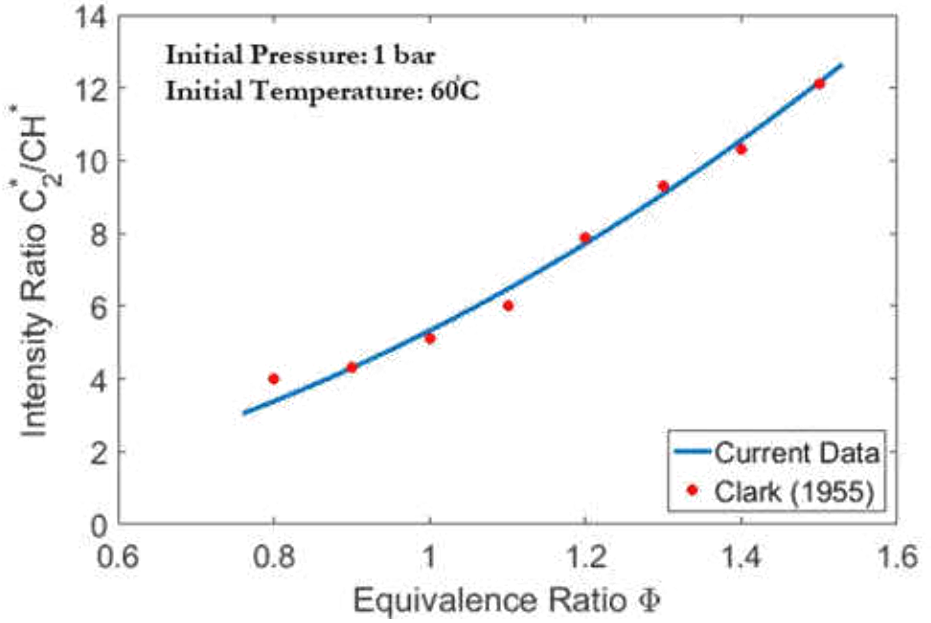

Figure 29: The average of the curve fits of the data obtained in Figure 9. The curve fit is compared to Clark's [9] iso-octane data. Clark's iso-octane data is scaled to be on the same order as the gasoline data since the measurement is fuel specific.

Figure 30 shows the various calibration curves at initial charge pressures of 1, 3, and 5 bar. Their average correlation coefficient show strong agreement and the average uncertainty in the

calculation of the intensity ratio across all cases and pressures was found to be ± 0.62. The intensity ratios were found to shift linearly with a negative slope. This trend was noticed in Figure 28 where the shift was an effect of the pressure rise due to combustion, whereas Figure 30 shows the effect of the initial charge pressure.

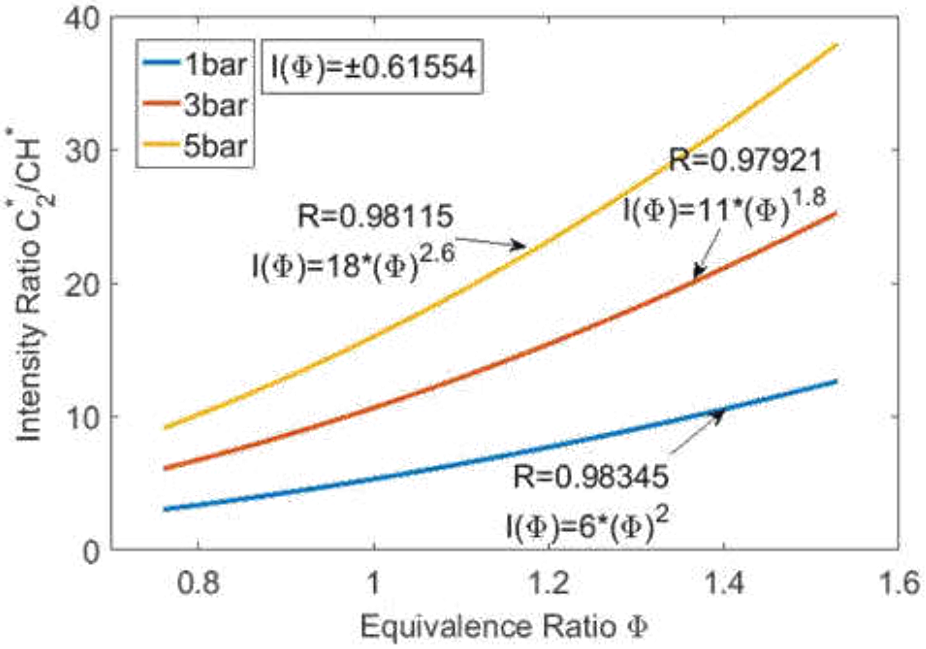

Figure 30: Calibration curves associated with charge pressures 1, 3, and 5 bar. The curve equation and correlation parameter are labeled for the respective curve fits.

For the 7 and 10 bar cases an unexpected trend was observed, see Figure 31. The lower charge pressure data showed positive power relations. The higher charge pressure data showed negative power relations. The correlation coefficients do not agrees as well as the lower charge pressures, but still show agreement comparable to what was seen in previous work [17], [29], [32], [36].

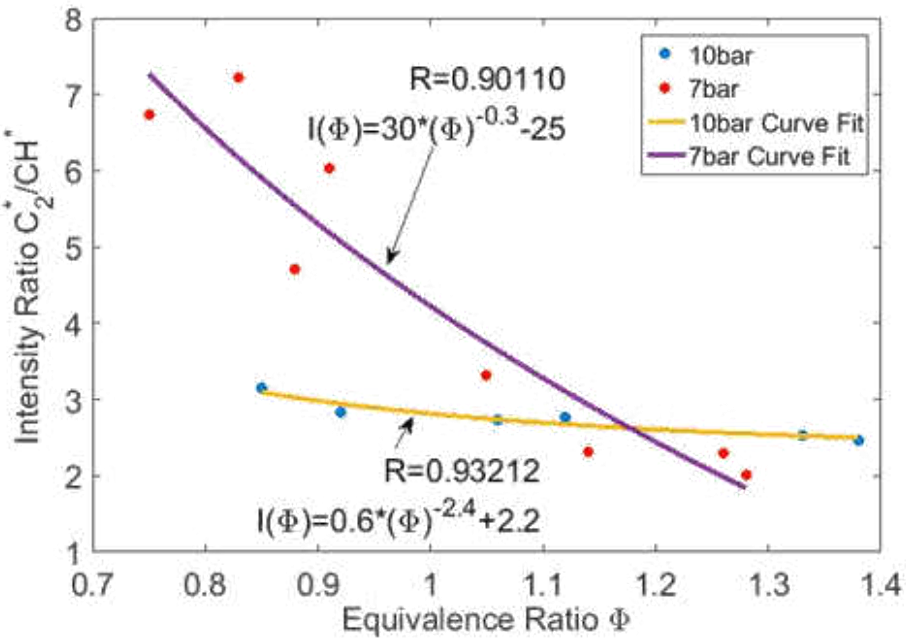

Figure 31: Calibration curves associated with charge pressures 7 and 10 bar. The curve equation and correlation parameter are labeled for the respective curve fits.

From the 5 calibration curves drawn at 1, 3, 5, 7 and 10 bar a relation was made correlating the intensity ratio of $\frac{C_2^*}{CH^*}$ to the equivalence ratio and initial charge pressure.

$$I(\Phi, P) = P * (a * (\Phi)^b + c) + d \quad (4)$$

Figure 32 shows a 3-dimensional representation of the relation in accordance with the data obtained for the gasoline fuel at the various charge pressure. This representation would be used as a calibration map for the measurement.

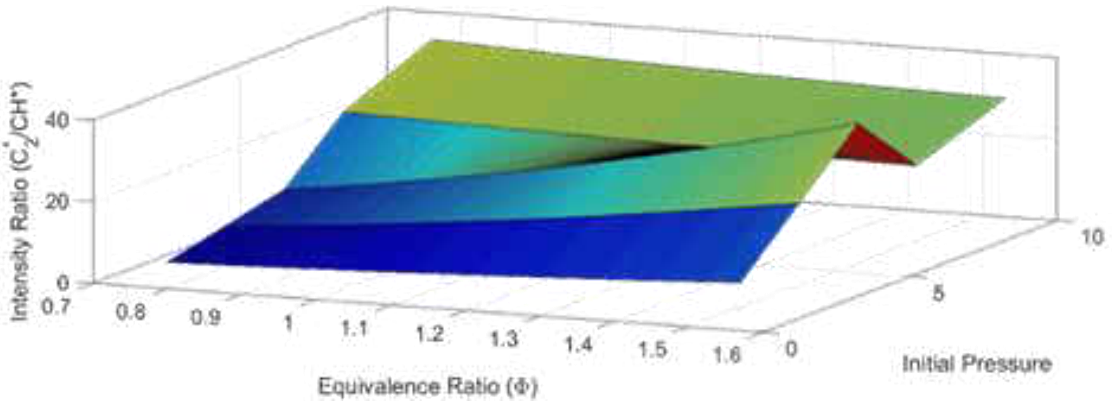

Figure 32: Hypothesized calibration map for gasoline for charge pressures between 1 and 10 bar drawn from equation 4.

CHAPTER SEVEN: CONCLUSION

It was shown that the initial charge pressure does influence the intensity ratio of $\frac{C_2^*}{CH^*}$ The individual calibration curves at the various charge pressures show good agreement as power curves. The intensity ratio of $\frac{C_2^*}{CH^*}$ was found to behave linearly with increasing charge pressure up to 5 bar. A relation was drawn relating the charge pressure and the equivalence ratio to the intensity ratio. The relation could be used as a means of back calculating the equivalence ratio and is useful for the calculation of local equivalence ratios.

The higher initial pressures of 7 and 10 bar returned a negative power relation. This was an unexpected occurrence, but is believed to be due to the increase in CH^* intensity increase with pressure [25], [33], [37]. Tinaut *et al.* [33] reported that CH^* emission intensity correlates directly with pressure increase, see Figure 33, while the same trend is not seen with C_2^*. It is expected that CH^* will at some point dominate the signal as the pressure is increased in terms of intensity [33], but C_2^* is still expected to dominate spatially [18]–[21], [25], [32]. The effects of these behaviors on the calibration map require further exploration.

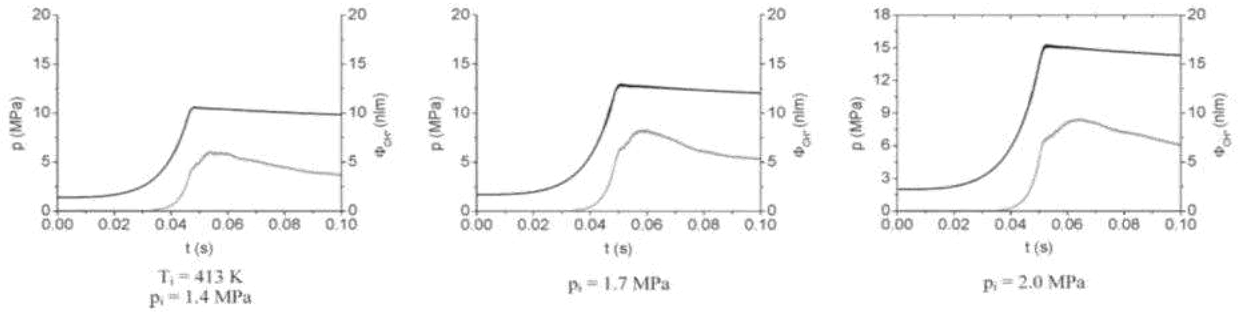

a.) b.) c.)

Figure 33: Simultaneous comparison of a pressure rise due to combustion and peak intensity of CH* at charge pressures of a.) 1.4, b.) 1.7, and c.) 2.0 MPa.

Source: [33]

LIST OF REFERNCES

[1] N. Loris, “EPA Formally Declares CO2 a Dangerous Pollutant.pdf,” *The Daily Signal*, The Daily Signal, p. 1, Dec-2009.

[2] A. V. Obe, “Carbon Dioxide Review: 1982,” *Interdiscip. Sci. Rev.*, vol. 9, no. 1, pp. 90–92, 1984.

[3] J. A. Kleypas, R. W. Buddemeier, D. Archer, J.-P. Gattuso, C. Langdon, and B. N. Opdyke, “Geochemical consequences of increased atmospheric carbon dioxide on coral reefs,” *Science (80-.).*, vol. 284, no. April, pp. 118–120, 1999.

[4] P. S. Curtis and X. Wang, “A meta-analysis of elevated CO2 effects on woody plant mass, form, and physiology,” *Oecologia*, vol. 113, no. 3, pp. 299–313, 1998.

[5] C. Beer, M. Reichstein, E. Tomelleri, P. Ciais, M. Jung, N. Carvalhais, C. Rodenbeck, M. A. Arain, D. Baldocchi, G. B. Bonan, A. Bondeau, A. Cescatti, G. Lasslop, A. Lindroth, M. Lomas, S. Luyssaert, H. Margolis, K. W. Oleson, O. Roupsard, E. Veenendaal, N. Viovy, C. Williams, F. I. Woodward, and D. Papale, “Terrestrial Gross Carbon Dioxide Uptake: Global Distribution and Covariation with Climate,” *Science (80-.).*, vol. 329, no. 5993, pp. 834–838, 2010.

[6] T. Zachariadis, “On the baseline evolution of automobile fuel economy in Europe,” *Energy Policy*, vol. 34, no. 14, pp. 1773–1785, 2006.

[7] I. . Dresselhaus, M.S.; Thomas, “Alternative energy technologies,” *Nature*, vol. 414, no. November, pp. 332–337, 2001.

[8] T. Sztanek, “Piston and Cylinder,” *Britannica*. p. 2, 2017.

[9] P. G. Aleiferis, Y. Hardalupas, A. M. K. P. Taylor, K. Ishii, and Y. Urata, "Flame chemiluminescence studies of cyclic combustion variations and air-to-fuel ratio of the reacting mixture in a lean-burn stratified-charge spark-ignition engine," *Combust. Flame*, vol. 136, no. 1–2, pp. 72–90, 2004.

[10] M. C. Drake, T. D. Fansler, and A. M. Lippert, "Stratified-charge combustion: Modeling and imaging of a spray-guided direct-injection spark-ignition engine," *Proc. Combust. Inst.*, vol. 30 II, no. 2, pp. 2683–2691, 2005.

[11] P. Sementa, B. Maria Vaglieco, and F. Catapano, "Thermodynamic and optical characterizations of a high performance GDI engine operating in homogeneous and stratified charge mixture conditions fueled with gasoline and bio-ethanol," *Fuel*, vol. 96, pp. 204–219, 2012.

[12] F. Zhao, M. C. Lai, D. L. Harrington, A. International, R. Journal, F. Zhao, and D. L. Harrington, "PROGRESS IN ENERGY AND Automotive spark-ignited direct-injection gasoline engines," *Prog. Energy Combust. Sci.*, no. 25, pp. 437–562, 1999.

[13] M. B. Çelik and B. Özdalyan, "Gasoline direct injection," no. Chapter 1, pp. 1–19, 2000.

[14] C. Benz, "Carburetor," United States Patent Office 382585, 1888.

[15] K. Nice, "How Fuel Injection Systems Work," *How Stuff Works*. p. 5, 2002.

[16] B. Liang, Y. Ge, J. Tan, X. Han, L. Gao, L. Hao, W. Ye, and P. Dai, "Comparison of PM emissions from a gasoline direct injected (GDI) vehicle and a port fuel injected (PFI) vehicle measured by electrical low pressure impactor (ELPI) with two fuels: Gasoline and M15 methanol gasoline," *J. Aerosol Sci.*, vol. 57, pp. 22–31, 2013.

[17] T. P. (Lewis F. P. L. Clark, “STUDIES OF OH, CO, CH, AND C2 RADIATION FROM LAMINAR AND TURBULENT PROPANE-AIR AND ETHYLENE-AIR FLAMES,” 1955.

[18] P.-E. BENGTSSON and M. ALDEN, “C2 Production and Excitation in Sooting Flames using Visible Laser Radiation: Implications for Diagnostics in Sooting Flames,” *Combust. Sci. Technol.*, vol. 77, no. 4–6, pp. 307–318, 1991.

[19] S. Karnani and D. Dunn-Rankin, “Visualizing CH* chemiluminescence in sooting flames,” *Combust. Flame*, vol. 160, no. 10, pp. 2275–2278, 2013.

[20] J. Kojima, Y. Ikeda, and T. Nakajima, “Spatially resolved measurement of OH*, CH *, AND C*\n2 chemiluminescence in the reaction zone of laminar methane/air premixed flames,” *Proc. Combust. Inst.*, vol. 28, pp. 1757–1764, 2000.

[21] P. Nau, J. Krüger, A. Lackner, M. Letzgus, and A. Brockhinke, “On the quantification of OH*, CH*, and C2* chemiluminescence in flames,” *Appl. Phys. B Lasers Opt.*, vol. 107, no. 3, pp. 551–559, 2012.

[22] N. Kawahara, A. Inoue, and E. Tomita, “Time-series Spectra Measurements from Initial Flame Kernel in a Spark-Ignition Engine,” *17th Int. Symp. Appl. Laser Tech. to Fluid Mech.*, no. Iccd, pp. 7–10, 2014.

[23] Y. Ikeda, T. Kurahashi, N. Kawahara, and E. Tomita, “Temperature Measurements of Laminar Propane / Air Premixed Flame Using Detailed OH* Spectra Intensity Ratio,” *12th Int. Symp. Appl. Laser Tech. to Fluid Mech.*, no. 1, pp. 1–11, 2004.

[24] C. S. Panoutsos, Y. Hardalupas, and A. M. K. P. Taylor, “Numerical evaluation of

equivalence ratio measurement using OH* and CH* chemiluminescence in premixed and non-premixed methane-air flames," *Combust. Flame*, vol. 156, no. 2, pp. 273–291, 2009.

[25] J. Kojima, Y. Ikeda, and T. Nakajima, "Basic aspects of OH(A), CH(A), and C2(d) chemiluminescence in the reaction zone of laminar methane-air premixed flames," *Combust. Flame*, vol. 140, no. 1–2, pp. 34–45, 2005.

[26] H. Edner and S. Svanberg, "Simultaneous , Spatially Resolved Monitoring of C 2 and OH in a C2H2 / O 2 Flame Using a Diode Array Detector," vol. 97, pp. 93–97, 1982.

[27] K. Matyjaszewski and T. P. Davis, *Handbook of Radical Polymerization*, no. January 2002. Wiley-Interscience, 2002.

[28] T. Chou and D. J. Patterson, "In-cylinder measurement of mixture maldistribution in a L-head engine," *Combust. Flame*, vol. 101, no. 1–2, pp. 45–57, 1995.

[29] D. Guyot, F. Guethe, B. Schuermans, A. Lacarelle, and C. O. Paschereit, "CH*/OH* Chemiluminescence Response of an Atmospheric Premixed Flame Under Varying Operating Conditions," *Vol. 2 Combust. Fuels Emiss. Parts A B*, pp. 933–944, 2010.

[30] T. S. CHENG, C.-Y. WU, Y.-H. LI, and Y.-C. CHAO, "Chemiluminescence Measurements of Local Equivalence Ratio in a Partially Premixed Flame," *Combust. Sci. Technol.*, vol. 178, no. 10–11, pp. 1821–1841, 2006.

[31] T. D. Fansler, B. Stojkovic, M. C. Drake, and M. E. Rosalik, "Local fuel concentration measurements in internal combustion engines using spark-emission spectroscopy," *Appl. Phys. B Lasers Opt.*, vol. 75, no. 4–5, pp. 577–590, 2002.

[32] A. P. Pimenta, "CH and C 2 Radicals Characterization in Natural Gas Turbulent Diffusion

Flames," *J. Braz. Soc. Mech. Sci. Eng.*, vol. XXVII, no. 2, pp. 110–118, 2005.

[33] F. V. Tinaut, M. Reyes, B. Gimenez, and J. V. Pastor, "Measurements of OH* and CH* chemiluminescence in premixed flames in a constant volume combustion bomb under autoignition conditions," *Energy and Fuels*, vol. 25, no. 1, pp. 119–129, 2011.

[34] S. L. Kokjohn and R. D. Reitz, "Investigation of the Roles of Flame Propagation, Turbulent Mixing, and Volumetric Heat Release in Conventional and Low Temperature Diesel Combustion," *J. Eng. Gas Turbines Power*, vol. 133, no. October 2011, pp. 1–10, 2011.

[35] B. T. Zigler, S. M. Walton, D. Assanis, E. Perez, M. S. Wooldridge, and S. T. Wooldridge, "An Imaging Study of Compression Ignition Phenomena of Iso-Octane, Indolene, and Gasoline Fuels in a Single-Cylinder Research Engine," *J. Eng. Gas Turbines Power*, vol. 130, no. 5, p. 52803, 2008.

[36] Y. K. Jeong, C. H. Jeon, and Y. J. Chang, "Evaluation of the equivalence ratio of the reacting mixture using intensity ratio of chemiluminescence in laminar partially premixed CH4-air flames," *Exp. Therm. Fluid Sci.*, vol. 30, no. 7, pp. 663–673, 2006.

[37] J. R. Kim, F. Akamatsu, G. M. Choi, and D. J. Kim, "Observation of local heat release rate with changing combustor pressure in the CH4/air flame (wrinkled laminar regime)," *Thermochim. Acta*, vol. 491, no. 1–2, pp. 109–115, 2009.

[38] P. S. Toh, "Image Acquisition System for Machine Vidsion Applications," United States Patent Office 6346966, 2002.

[39] M. Aggarwal and N. Ahuja, "Split aperture imaging for high dynamic range," *Proc.*

Eighth IEEE Int. Conf. Comput. Vision. ICCV 2001, vol. 2, no. 1, pp. 7–17, 2001.

[40] J.-M. SAMANIEGO, F. N. EGOLFOPOULOS, and C. T. BOWMAN, "CO_2 * Chemiluminescence in Premixed Flames," *Combust. Sci. Technol.*, vol. 109, no. 1–6, pp. 183–203, 1995.